UCLA
UCLA Electronic Theses and Dissertations

Title
Decoding the genome of disordered materials

Permalink
https://escholarship.org/uc/item/32h488wr

Author
Zhou, Qi

Publication Date
2022

Peer reviewed|Thesis/dissertation

UNIVERSITY OF CALIFORNIA

Los Angeles

Decoding the Genome of Disordered Materials

A dissertation submitted in partial satisfaction

of the requirements for the degree

Doctor of Philosophy in Civil Engineering

by

Qi Zhou

2023

ABSTRACT OF THE DISSERTATION

Decoding the Genome of Disordered Materials

by

Qi Zhou

Doctor of Philosophy in Civil Engineering

University of California, Los Angeles, 2023

Professor Mathieu Bauchy, Chair

Despite their critical role in various technological applications (e.g., optical fibers, display application, nuclear waste immobilization, etc.), the atomic structure of silicate glasses remains only partially understood. This is largely since, although conventional experiments (e.g., nuclear magnetic resonance, neutron or X-ray diffraction, etc.) offer useful "fingerprints" of the glass structure (e.g., pair distribution function, coordination numbers, etc.), they do not provide direct access to the atomic structure itself (i.e., the cartesian positions of the atoms). Indeed, although experimental data offer important constraints on the glass structure, these constraints cannot uniquely define the structure itself. For instance, a virtually infinite number of very different structures can present the same pair distribution function.

Atomistic simulations can offer direct access to the atomic structure of glasses, which is otherwise invisible from conventional experiments. However, molecular dynamics (MD) simulations of glasses based on the melt quenching technique remain plagued by the use of high cooling rates, while reverse Monte Carlo (RMC) modeling can yield non-unique solutions. Here, we adopt the force-enhanced atomic refinement (FEAR) method to overcome

these limitations and decipher the atomic structure of a sodium silicate glass. We show that FEAR offers an unprecedented description of the atomic structure of sodium silicate, wherein the simulated configuration simultaneously exhibits enhanced agreement with experimental diffraction data and higher energetic stability as compared to those generated by MD or RMC. This result allows us to reveal new insights into the atomic structure of sodium silicate glasses. Specifically, we show that sodium silicate glasses exhibit a more ordered medium-range order structure than previously suggested by MD simulations. These results pave the way toward an increased ability to accurately describe the atomic structure of glasses.

Upon a change in temperature, non-crystalline solids exhibit some variation in their volume—which is captured by their coefficient of thermal expansion. In that regard, glassy silica—an archetypical oxide glass—exhibits an anomalously low bulk thermal expansion, which is more than an order of magnitude lower than the thermal expansion of the interatomic bonds within its atomic network. Here, by combining in-situ neutron diffraction experiments and force-enhanced atomic refinement simulations, we investigate the effect of temperature on the atomic structure of glassy silica at various scales. We reveal that the low thermal expansion of glassy silica is governed by a compaction of the shape of the silicate rings in the medium-range order, which counterbalances the interatomic expansion in the short-range order.

On the other hand, Silicate glasses have no long-range order and exhibit a short-range order that is often fairly like that of their crystalline counterparts. Hence, the out-of-equilibrium nature of glasses is largely encoded in their medium-range order. However, the ring size distribution—the key feature of silicate glasses' medium-range structure—remains invisible to conventional experiments and, hence, is largely unknown. Here, by combining neutron diffraction experiments and force-enhanced atomic refinement simulations for two archetypical silicate glasses, we show that rings of different sizes exhibit a distinct contribution to the first sharp diffraction peak in the structure factor. Based on these results, we demonstrate that the ring size distribution of silicate glasses can be determined solely from

neutron diffraction patterns, by analyzing the shape of the first sharp diffraction peak. This method makes it possible to uncover the nature of silicate glasses' medium-range order.

Overall, FEAR refinement yields a silicate glass structure that simultaneously exhibits enhanced agreement with diffraction data and higher energetic stability as compared to configurations generated by MD, RMC, or HRMC. As such, FEAR offers an unprecedented description of the atomic structure of sodium silicate glasses. We find that the enhanced thermodynamic stability offered by FEAR primarily finds its roots in the Qn and ring size distributions of the network. Our findings thus suggest that the structure of silicate glasses is more ordered, less random than previously suggested by MD simulations. Overall, this study establishes FEAR as a promising tool to explore the complex, largely hidden atomic structure of disordered solids.

The dissertation of Qi Zhou is approved.

Gaurav Sant

Laurent G. Pilon

Sanjay K. Mohanty

Mathieu Bauchy, Committee Chair

University of California, Los Angeles

2023

To my parents . . .

who—among so many other things—

saw to it that I loved SCIENCE

while I was still in elementary school

TABLE OF CONTENTS

LIST OF FIGURES

x

LIST OF TABLES

ACKNOWLEDGMENTS

First and foremost, I would like to express my sincere gratitude to my advisor, Professor Mathieu Bauchy, for his guidance and generous support over the past five years. The completion of this dissertation would not be possible without his insight and mentorship.

I would also like to thank Professor Gaurav Sant, Professor Sanjay Mohanty, and Professor Laurent Pilon for serving on my committee, providing guidance and suggestions that are vital for the completion of this dissertation.

I am grateful to all current and past members of the Physics of Amorphous and Inorganic solids laboratory whom I have had the pleasure to work with during this and other related projects. I am indebted to Dr. Tao Du, Dr. Longwen Tang, Dr. Yu Song, Mrs. Ying Shi, Ms. Ruoxia Chen, Mr. YuHai Li, Mr Kai Yang, I would also like to extend my appreciation to my collaborators at UCLA's Civil and Environmental Engineering department. You all helped me to keep things in perspective and maintain a healthy stress level.

Finally, I want to thank my parents Mr. Xiaonan Zhou, Mrs Xia Mu, my dearest Mr. Zhou Li.

2014	B.S. (Materials Science and Engineering), Central South University, Changsha, China.
2016	M.A. (Materials Science and Engineering), Columbia University, New York City, NY.
2020	Intern, CORNING INC., Corining, NY.
2016–2022	PhD Candidate, Physics of AmoRphous and Inorganic Solids Laboratory, UCLA, Los Angeles, CA.

PUBLICATIONS

Zhou, Qi, et al. *Revealing the medium-range structure of glassy silica using force-enhanced atomic refinement.* Journal of Non-Crystalline Solids 573 (2021): 121138.

Zhou, Qi, et al. *Experimental method to quantify the ring size distribution in silicate glasses and simulation validation thereof.* Science advances 7.28 (2021): eabh1761.

Zhou, Qi, et al. *Role of internal stress in the early-stage nucleation of amorphous calcium carbonate gels.* Applied Sciences 10.12 (2020): 4359.

Zhou, Qi, et al. *New insights into the structure of sodium silicate glasses by force-enhanced atomic refinement.* Journal of Non-Crystalline Solids 536 (2020): 120006.

CHAPTER 1

Introduction

The physical properties of materials are determined by their atomic structure. By relating the experimental data with the structure, we could understand the properties of certain structures[1]. However, the desired information is not easy to obtain because for glass, cementitious materials and liquid, structural disorder leads to complexity. To facilitate progress at a large scale and exploit the unique properties that these materials may offer, the understanding of atomic-level structure is necessary, and the boundaries of amorphous material engineering technology has to be pushed forward[2-5].

As one of the most vital and influential materials, glass becomes essential to our daily life[1]. Throughout the history, the understanding for glass was mostly empirical. Recent years, theoretical and experimental advances help us built a more rigorous scientific principles on glass science. On the other hand, applications of glass become more and more impactful. Modern high-tech glasses like electrochromic windows can improve energy efficiency for applications in transportation. Strengthened glasses with high chemical durability have been critical for healthcare applications such as pharmaceutical packaging. These advancements not only offer a remarkable level of understanding but also contribute to the atomic level design of novel functional glasses. Atomic-level descriptions of the glassy state are complex due to the lack of long-range order that we found in crystalline materials 6. Since there are infinite combinations of compositions can give us successful glass formation, nearly every element of the periodic table can be incorporated into a glass. it is difficult to understand all the possible structures. Our understanding of glass structure and properties

is also blocked due to the non-equilibrium thermodynamic state of glass. Glass is continually relaxing from this non-equilibrium state toward a metastable or stable liquid phase. Such transition and relaxation effects play an essential role in determining the property evolution of all glass compositions. Despite of the grand progress in understanding glass transition and relaxation phenomena, the structural origins for such relaxation modes in glass remain unclear[7].

Different from glass, crystalline solid is a material with atoms that are arranged in a highly ordered microscopic structure. By forming a crystal lattice that extends in all directions, crystal has a periodic arrangement, and through X-rays characterization, we can observe the so called "Bragg diffraction". These diffraction peaks are sharply defined and when we analyze with a wave theory of the X-rays, lead to clear evidence of periodic order in the crystalline state[8]. We can understand the full structure of the crystal by analyzing the diffraction angles at which the peaks appeared and the wavelength of the X-rays. Here, the X-ray structure factor of a single crystal consists of a sequence of sharp peaks. If cooled fast enough, the crystallization of a liquid can be avoided, the system accesses the metastable supercooled liquid state. In contrast with crystals, amorphous materials and liquids have smooth peaks, thus provides less specific structure information[5]. This is due to the lack of long-range order within the structure in amorphous state. Owing to this non-crystalline structure, glass does not need to satisfy the same stoichiometric requirements as in crystal chemistry. Yet it is obvious that there are some well-defined local structures on the nanometer scale[3,9]. Often, such local structure is important for some physical properties. Since the composition of glass can be continuously adjustable, the properties can also be change during the relaxation, opening the possibilities for refined combinations of properties. This presents a far more difficult problem of structural determination of amorphous solids that need new tools.

As I mentioned above, one of the main problems of glass science is to relate its complicated compositions and time dependence of glass properties. Recently, a popular and

natural approach to address the problem is to apply the computer simulations, either with conventional Molecular dynamics simulations or Monte Carlo method 4,9,10, along with the suitable interatomic potentials. Classical molecular dynamics have proved to be a useful tool in studying the properties of amorphous materials like silicate glasses, which are not always easily accessible from experiments. Silica-based glasses have great importance in various technological fields11–15. With the combination of advanced techniques like X-ray absorption fine structure, neutron diffraction, and molecular dynamics simulations, we can reveal the structural features of certain glass compositions. Since MD simulations can provide some valuable details about the atomic mechanism which cannot be observed with experiments, we investigate the early-age precipitation of an amorphous calcium carbonate gel. Calcium carbonate is ubiquitous in nature and plays an important role in biomineralization, it is a common binding phase formed by organisms that produce an exoskeleton. Large amount of carbon dioxide flows into the atmosphere and has becomes a hazard primarily due to their greenhouse gas effect2,16,17. Thus, understanding the mechanism for precipitation of calcium carbonate becomes the key for carbon dioxide utilization and provides a promising route to turn carbon dioxide into a resource like concrete binders. Although the existence of some stable prenucleation clusters has been suggested, the atomic scale mechanism of calcium carbonate in aqueous condition remains largely unknown2,18,19. The precipitation of amorphous calcium carbonate is barrierless in supersaturated calcium carbonate solutions and does not follow conventional nucleation pathways Although MD simulations are limited to small systems and timescales, they can offer us a direct access to the time-dependent structure and properties of disordered materials based on an accurate forcefield. From the molecular positions, the forces acting on each molecule are calculated, these are used to advance the positions and velocities through as mall timestep, and then the procedure is repeated.

However, one serious question regarding the reliability of MD simulations is that the cooling rate used in simulations for glass is much higher than that typically achieved exper-

imentally. We need more powerful tools to improve the ability to predict properties such as mechanical strength, elastic constants, chemical durability, and conductivity in order to meet some specific need or applications. Similar to silicate glass, the X-ray diffraction pattern from Calcium–silicate–hydrates (C¬–S–H) have shown to exhibit only a few broad and weak diffraction maxima, it has been described as an amorphous material20–22. C–S–H is the main hydration product in cementitious systems, and it is the binding phase in the paste. Thus, it is important to understand the structure to control its strength, durability and creep properties. Such understanding requires an accurate description of the atomic structure of C–S–H, which is presently lacking. In contrast with the X-ray pattern, most experimental studies suggest that its structure is close to the one of tobermorite despite of different compositions. Previous studies have proven that C–S–H has a structure closer to the one of a glass than to the one of a crystal.

Alternatively, non-physics-based modeling approaches have been proposed to refine the atomic structure of disordered materials based on experimental data only. The most popular approach is the Reverse Monte Carlo (RMC) method. We can invert the diffraction data by "Reverse Monte Carlo" (RMC) 23or other methods without applying any interatomic potential but relies on information only. RMC modelling is a general method of structural modeling based on experimental data. Many different types of data and systems can be modelled. It is a variation of the standard Metropolis Monte Carlo (MMC) method. By producing a structural model that is consistent with one or several sets of experimental data and also a set of constraints like force or potential energy. To this end, diffraction data are commonly used as they offer a description of the short- and medium-range order atomic structure of disordered materials. Despite its wide use, the RMC methods comes with some serious limitations and often fails to predict a realistic atomic structure for non-crystalline solids. This comes from the fact that a virtually infinite number of distinct atomic structure can yield the same PDF—so that obtaining a good agreement between simulated and experimental PDF is not sufficient to ensure that the structure is realistic24. Here, the

4

experimental data provide incomplete information about the correlations between atoms. The atomics coordinates in the simulated model are of themselves of no direct interest. We want to make sure the models are useful. That is to say, RMC modelling is a method of structural modelling, we need the models help us understand some important aspect of the materials, like the relationship between structure and some physical properties. Afterall, it is important to have models that are both quantitatively predictive and broadly applicable across the large range of possible compositions. Here, we adopt (and optimize) an atomic structure refinement method recently proposed by Drabold et al.25, called force-enhanced atomic refinement (FEAR). This new method consists in combining RMC (to ensure that the simulated structure matches with experimental data) with some energy minimization (to ensure that the simulated system is as energetically stable as possible). In details, the initial structure is first optimized by RMC. The resulting structure is then subjected to an energy minimization (EM, using the conjugate gradient method) to ensure the stability of the system. Here, we refine the original FEAR method by optimizing the enthalpy rather than the potential energy, that is, by allowing the system to adjust its volume and shape to release the presence of stress, if any. The RMC and RM steps are then iteratively repeated until convergence is obtained. The different steps of this refinement method are summarized in Figure below. Unlike alternative hybrid approaches—wherein structure and energy are optimized simultaneously—the interatomic forces are here only computed during the EM steps, which results in an improved computational efficiency. In addition, the present method does not rely on any assumption regarding the weight attributed to structure and energy during the optimization.
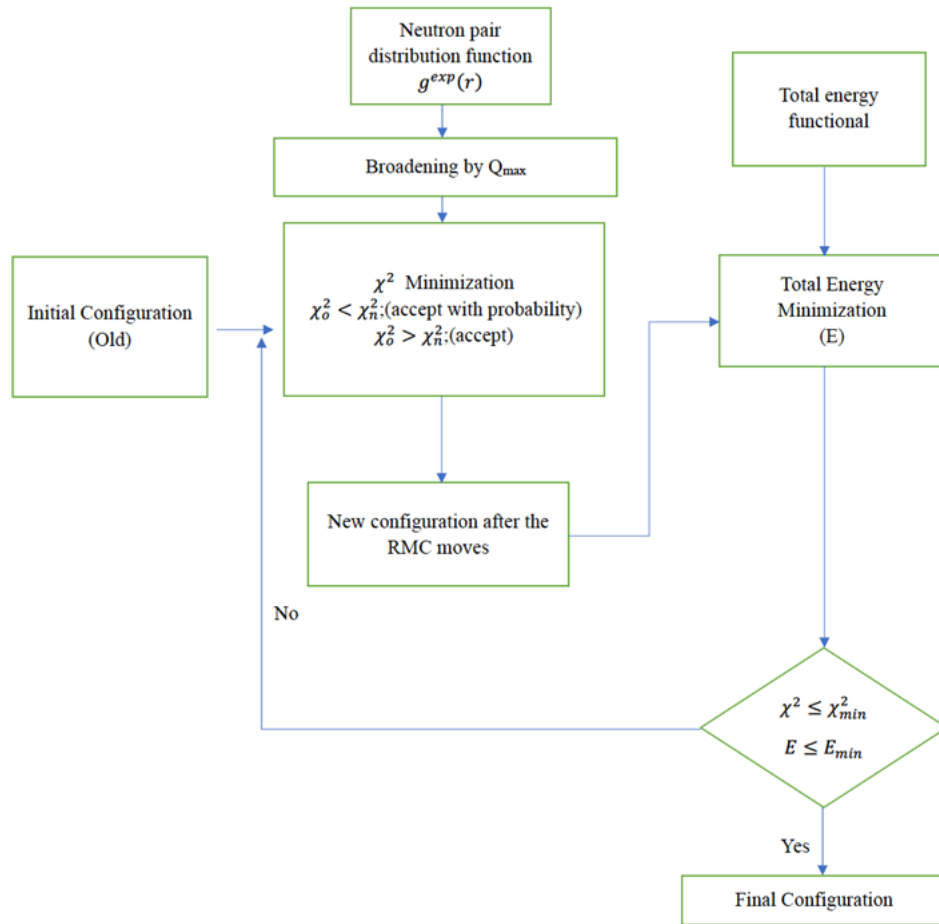
Figure 1.1: A schematic diagram of the atomic structure refinement method used herein.

CHAPTER 2

Revealing the Medium-Range Structure of Glassy Silica using Force-Enhanced Atomic Refinement

Despite the ubiquity and technological importance of silicate glasses 26–29, their atomic structure remains only partially understood 30. In that regard, even the structure of pure glassy silica (SiO2) remains subject to debate 31. The short-range order base structure of SiO2 is well understood, with SiO4 tetrahedral units that are interconnected via bridging-oxygen atoms 32. At larger distances, the SiO4 polytopes form some closed-loop rings, which largely dictates silica's medium-range order 10,33. However, even basic features of silica's medium-range order (e.g., ring size distribution) remain debated 34,35.

This lack of knowledge regarding the atomic structure of glassy silica—especially at the medium-range order—partially arises from the lack of experimental techniques that can directly probe the atomic structure of silicate glasses 36, although recent developments offer exciting perspectives in that regard 37. Indeed, even though conventional experiments can offer useful "fingerprints" of the glass structure, they often do not provide a direct access to the atomic structure itself 38. For instance, diffraction experiments offer some signatures of the medium-range order of silicate glasses, e.g., as captured by the first-sharp diffraction peak (FSDP) 39–41. Although this information places some constraints on the nature of the medium-range order, it does not directly reveal the medium-range order structure itself—e.g., it does not provide a direct access to the ring size distribution 42.

As an alternative route to experiments, atomistic simulations offer a direct and full access to the atomic structure of glasses 14,43,44 and, hence, can reveal some atomic details that

are invisible to conventional experiments 14,31,45. However, atomistic simulations come with their own challenges and limitations 46,47. On the one hand, molecular dynamics (MD) simulations solely rely on the knowledge of the interatomic forcefield. Following the melt-quench method, melts are equilibrated at high temperature to lose the memory of their initial configuration and subsequently quenched to the glassy state with a high cooling rate 13,44,48. Although this melt-quenching approach roughly mimics the experimental synthesis protocol of glasses, MD simulations are limited to very large cooling rates (typically 102 to 10-2 K/ps) due to their computational cost 49. This is a serious limitation since, as out-of-equilibrium materials, the structure and properties of glasses depend on their thermal history 13. In that regard, glasses simulated by MD using the conventional melt-quench approach typically exhibit a larger fictive temperature than their experimental counterparts, which, in turn, causes their structure to be unrealistically disordered (especially at the medium-range order) 44,46,48,50–54. On the other hand, conventional reverse Monte Carlo (RMC) simulations solely rely on the knowledge of some experimental constraints (e.g., experimental pair distribution function) 23,24,55. As a key advantage, RMC simulations can yield glasses structures that are compatible with such constraints while bypassing the melt-quenching route, thereby avoiding the issue of the cooling rate 56–59. However, a RMC simulation remains an ill-defined problem, since, for instance, numerous atomic structures can exhibit the same pair distribution function 60. As such, glass structures that are generated by RMC typically exhibit an excellent agreement with the experimental data that are used as constraints during the refinement, but may nevertheless be fairly unrealistic (e.g., showing extremely high potential energy) 61. Overall, these challenges limit the ability of atomistic simulations to provide fully trustable atomic structures for silicate glasses.

To address this challenge, Drabold et al. recently introduced a new atomic refinement approach that seamlessly combine the knowledge of (i) the interatomic forcefield (which is typically used by MD simulations) and (ii) experimental constraints (which are typically used by RMC simulations) 25. In detail, Drabold's force-enhanced atomic refinement (FEAR)

method relies on an iterative combination of sequential RMC refinements and energy minimizations 25,38,61,62. Unlike hybrid RMC approaches—which simultaneously refine the experimental constraints and minimize the energy through a single, unified cost optimization function accounting for both experimental constraints and energy—FEAR does not rely on any arbitrary choices regarding the weights attributed to energy and experimental constraints. The fact that the energy of the system is only computed during the energy minimizations steps (rather than at every step in hybrid RMC approaches) also results in enhanced overall computational efficiency 25.

Recently, we demonstrated that FEAR yields an atomic structure for a sodium silicate glass that is more realistic than that offered by MD or RMC 61. In this contribution, we extend this approach to the archetypical case of glassy silica. Indeed, despite its apparent simplicity as compared to modified silicate glasses like sodium silicate, glassy silica comes with unique challenges. In particular, the structure and properties of silica have been shown to be more affected by the cooling rate than those of sodium silicate 63. Here, we show that the SiO2 structure generated by FEAR simultaneously (i) exhibits an excellent agreement with experimental data and (ii) is more energetically stable than those obtained by MD or RMC simulations. This allows us to investigate the nature of the medium-range order structure in glassy silica.

2.1 Method

In the following, we compare the ability of MD, RMC, and FEAR to offer a realistic description of the atomic structure of glassy silica, which is an archetypical model glass and offers a structural basis for more complex modified silicate glasses. The simulated system comprises 3000 atoms. For this system, we adopt the Beest–Kramer–Santen (BKS) forcefield 64, which has been extensively used to investigate the structure, dynamics, and thermodynamics of silica 44,48,63. In line with previous studies, we use a cutoff of 5.5 Å and 10.0 Å for the short-range and long-range Coulombic interactions, respectively 48,65. The long-range Coulombic interactions are evaluated with the Particle-Particle Particle Mesh

(PPPM) algorithm 66 with an accuracy of 10-5—wherein the PPPM approach relies on the particle mesh method, which consists of interpolating the particles onto a three-dimensional grid for improved computational efficiency.

In order to further assess whether or not the outcome of the FEAR method depends on the choice of the interatomic potential (i.e., BKS) used during the energy minimizations, we repeat the FEAR simulations while using selected alternative forcefields, namely, the interatomic potentials from Guillot-Sator 67 and Pedone et al. 68 et al. We select these potentials as, although they all present a two-body formulation, they rely on different analytical forms, different parameterizations, and different partial charges (i.e., the charges attributed to Si and O atoms). Note that, to ensure consistency, all the other simulation parameters are kept identical. All simulations are carried out using the Large-scale Atomic/Molecular Massively Parallel Simulator (LAMMPS) package 69

2.2 Melt-quenching simulations by molecular dynamics (MD)

To establish benchmark silica structures that can be compared with that generated by FEAR, we first prepare a series of glassy silica structures by melt-quenching using MD simulations, as detailed in the following. An initial silica configuration is first created by randomly placing the atoms in a cubic box while ensuring the absence of any unrealistic overlap. The system is then melted at 5000 K under zero pressure in the isothermal-isobaric (NPT) ensemble for 100 ps to ensure the complete loss of the memory of the initial configuration. The melt is then linearly cooled down to 300 K under zero pressure in the NPT ensemble with varying cooling rates ranging from 102 down to 10–2 K/ps. For all simulations, we adopt the Nosé–Hoover thermostat and a fixed timestep of 1 fs 70.

2.3 Reverse Monte Carlo (RMC) simulations

As a second benchmark, we then use experimental neutron diffraction data 71 to create a glassy silica structure by RMC simulation 23,55, as implemented through an in-house fix in LAMMPS. This method iteratively refines the position of the atoms in a simulation box until the glass exhibits a structure that matches target experimental data—here, we use the

neutron pair distribution function (PDF) sourced from Ref. 71 as experimental constraint. To compare the simulated structure with neutron diffraction data, we first calculate the neutron PDF $g_N(r)$ of the simulated structures by combining the partial PDFs $g_{ij}(r)$ as:

$$g_N(r) = \frac{1}{\sum_{i,j=1}^{n} c_i c_j b_i b_j} \sum_{i,j=1}^{n} c_i c_j b_i b_j g_{ij}(r) \tag{2.1}$$

where c_i are the molar fractions of element i (i = Si or O), b_i are the neutron scattering lengths of the species 72 (equal to 4.1491 and 5.803 fm for Si and O atoms, respectively), and r is the real-space distance. Note that, to ensure a meaningful comparison between simulated and experimental PDFs, the simulated PDFs need to be broadened 73. Here, this is achieved by convoluting the computed PDFs with a normalized Gaussian distribution with a full width at half-maximum (FWHM) given by FWHM = 5.16/Qmax 13, where Qmax is the maximum wave vector used in the diffraction test (here, Qmax = 50 Å-1). The level of agreement between the simulated and experimental PDFs is then captured by the R_χ factor proposed by Wright (which is here calculated over r = 0-to-10 Å) 73:

$$R_\chi^2 = \sum_i [g^{exp}(r_i) - g^{sim}(r_i)]^2 / \sum_i [g^{exp}(r_i)]^2 \tag{2.2}$$

The RMC method is used to "invert" the experimental neutron pair distribution into a three-dimensional atomic structure. This method includes the following steps. (i) Starting from an initial random structure (identical to that used for the MD simulation), we first calculate the pair distribution function of the simulated structure and the Wright's coefficient R_χ^{old} (see Eq. 2). (ii) An atom is randomly selected and then displaced with a random direction and distance. (iii) The pair distribution function of the new configuration and the new coefficient R_χ^{new} are calculated. (iv) Following the Metropolis algorithm, the new configuration is accepted if $R_\chi^{new} \leq R_\chi^{old}$, that is, if the level of agreement between simulated and experimental structure is improved by the Monte Carlo move. If not, the atomic displacement is accepted

11

with a certain probability P shown below or refused otherwise:

$$P = exp[-\frac{R_\chi^{new2} - R_\chi^{old2}}{T_\chi}] \qquad (2.3)$$

where T_χ plays the role of a (unitless) "effective temperature" that controls the probability of acceptance (that is, higher values of T_χ result in higher probability of acceptance of the Monte Carlo moves). Here, the term $\frac{R_\chi^{new2} - R_\chi^{old2}}{T_\chi}$ is equivalent to the quantity $(U^{new} - U^{old})/kT$ in the conventional energy-based Metropolis algorithm, where U is the energy of the system—wherein, here, the Wright's coefficient R_χ plays the role of an "effective energy." Here, we use $T_\chi = 0.01$, which is found herein to result in the lowest final R_χ value upon convergence. Atomic displacements and directions are randomly chosen, with a uniform displacement probability distribution between 0 and 0.2 Å. The simulation box size is kept fixed throughout the simulation, with a length of 35.248 Å, so that density is fixed according to the experimental value of 2.20 g/cm3. A total number of 140,000 RMC moves are attempted until convergence.

2.4 Force-enhancement atomic refinement (FEAR) simulation

   Finally, we assess the ability of the FEAR refinement method to offer an improved description of the atomic structure of glassy silica as compared to those generated by MD or RMC. To this end, we adopt the FEAR methodology introduced by Drabold et al.25, which is here implemented via an in-house fix in LAMMPS. It should be noted that there exist some RMC-based approaches that are more elaborated than the one used herein. For instance, the hybrid reverse Monte Carlo approach (HRMC) consists in explicitly adding the computed potential energy of the system as an additional contribution in the RMC cost function to be minimized56,57. Although such advanced approaches can likely offer accuracies that are competitive with that offered by FEAR 61, FEAR presents two key advantages: (i) it is more computationally efficient since the energy does not need to computed at every RMC step and (ii) it does not rely on any assumption regarding the weights associated with the structural

and energy terms in the cost function. To ensure a meaningful comparison between FEAR, RMC, and MD, all simulated systems have the same size, and all simulation parameters are kept identical (e.g., forcefield, cutoff, etc.). In detail, we first start from a "randomized" structure generated by RMC while using a very high effective temperature, namely, $T_\chi = 5000$. Following the original implementation of the FEAR method, the system is then iteratively subjected to a combination of RMC refinements and energy minimization steps, wherein each FEAR iteration consists of (i) 3000 RMC steps and (ii) an energy minimization (conducted with the conjugated gradient method). We find that 20 of such iterations are sufficient to achieve a convergence of potential energy and R_χ for glassy silica. During the refinement, we dynamically adjust the average acceptance probability of the Metropolis algorithm by linearly decreasing the effective temperature T_χ from 10^3 down to 10^{-4} during the course of the FEAR refinement. These parameters are found to yield a glass structure exhibiting minimum R_χ and potential energy values.

2.5 Short-range order structural analysis

We analyze the short-range order radial environment around each atom by computing the partial PDFs. In addition, we explore the short-range angular environment of the atoms by computing the partial bond angle distribution (PBAD) using the RINGS package 74. Specifically, we focus on the O–Si–O and Si–O–Si PBADs, which characterize the intra- and inter-polytope angular structure of the SiO4 tetrahedral units, respectively. The distance cutoff used to define the Si–O bonds is chosen as the position of the first minimum after the first peak of the partial Si–O PDF (1.90 Å).

2.6 Medium-range order structural analysis

To further explore the structure of glassy silica over intermediate length scales, we calculate the partial structure factors $S_{ij}(Q)$ from the Fourier transform of the partial PDFs:

$$S_{ij}(Q) = 1 + \rho_0 \int_0^R 4\pi r^2 (g_{ij}(r) - 1) \frac{\sin(Qr)}{Qr} dr \qquad (2.4)$$

where Q is the scattering vector, ρ_0 is the average atomic number density, and R is the integration cutoff (half of the simulation box length). The total neutron structure factor is then evaluated by combining the partial structure factors as follows:

$$S_N(Q) = (\sum_{i,j=1}^{n} c_i c_j b_i b_j)^{-1} \sum_{i,j=1}^{n} c_i c_j b_i b_j S_{ij}(Q) \tag{2.5}$$

To further magnify high-Q fluctuations in the structure factor, we then calculate the reduced structure factor:

$$F(Q) = Q[S(Q) - 1] \tag{2.6}$$

Finally, to further explore the medium-range order structure of glassy silica, we compute the ring size distribution of each simulated system by using the RINGS package 74, wherein rings are defined as the shortest closed paths within the glassy silica network. The size of a ring is here defined in terms of the number of Si atoms it comprises. Here, we use the Guttman definition for the calculation 75. This definition was chosen as it yields, on average, the expected value of 6 rings per Si atom 42,51. We adopt a maximum ring size of 7, since no larger rings are found in the simulated structures (with the Guttman criterion).

3. Results

3.1 Evolution of structure upon force-enhanced atomic refinement

Figure 1 shows selected snapshots of the atomic structure of the simulated silica glass upon FEAR refinement. Si–O bonds (i.e., when the distance between a Si/O pair of atoms is lower than the 1.9 Å cutoff) are shown as edges in the snapshots. We observe that, the degree of connectivity (i.e., the number of Si–O bonds) increases during refinement.

Figure 2a shows the neutron PDF of the three structures shown in Fig. 1, that is, after different increasing numbers of FEAR refinement steps. The computed PDFs exhibit all the typical features that are expected for an SiO2 glass, namely, (i) a first peak around 1.6 Å that corresponds to Si–O correlations, (ii) a second peak around 2.7 Å associated to O–O correlations, and (iii) a plateau toward 1 at long r-distance, which is indicative of the
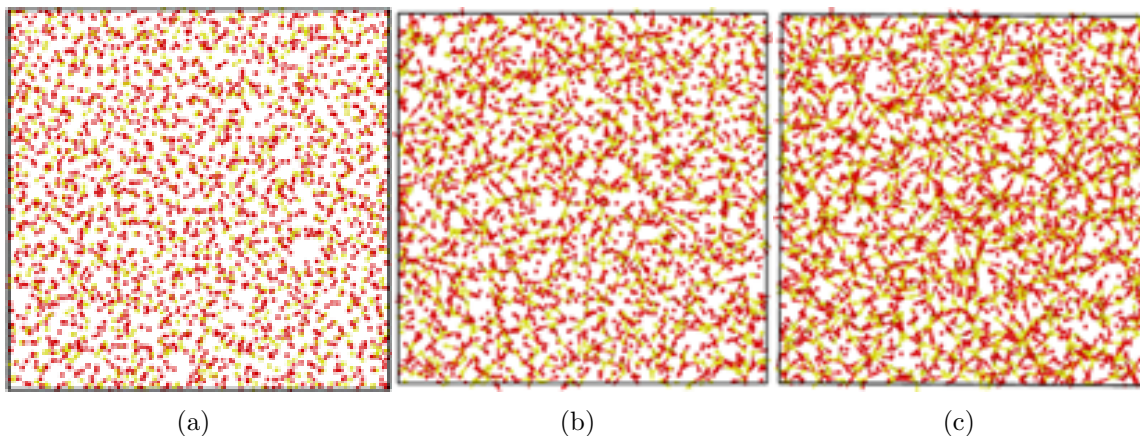
Figure 2.1: Snapshots of the simulated glassy silica structures obtained after (a) 1, (b) 10, and (b) 20 iterations of force-enhanced atomic refinement (FEAR). Si–O bonds (i.e., when the distance between a Si/O pair of atoms is lower than the 1.9 Å cutoff) are shown as edges.

absence of any long-range order. Overall, all these PDFs show a fair agreement with available experimental neutron diffraction data 71 in terms of the positions of the first and second peaks. This indicates that, even at early stage of the FEAR refinement, the simulated structures exhibit a realistic description of the interatomic distances in SiO4 tetrahedra. Nevertheless, we observe that, initially, the peaks of the computed PDF are notably broader than those of the experimental PDF. This indicates that, initially, the simulated structure is unrealistically disordered. Upon FEAR refinement, we observe that the shape of the first peak becomes reasonably well described (in terms of position, intensity, and width) after about 10 FEAR iterations, whereas the second peak becomes well reproduced after about 15 FEAR iterations. This suggests that the short-range order (i.e., low-distance correlations) is refined faster than the medium-range order (i.e., intermediate-distance correlations). This can be understood from the fact that refining the short-range order only involves some slight displacements of the neighbors of each atom, which only requires small energy barriers to be overcome. In contrast, refining the medium-range order requires some collective atomic displacements, including the breakage and formation of interatomic bonds, which requires hopping over higher energy barriers.
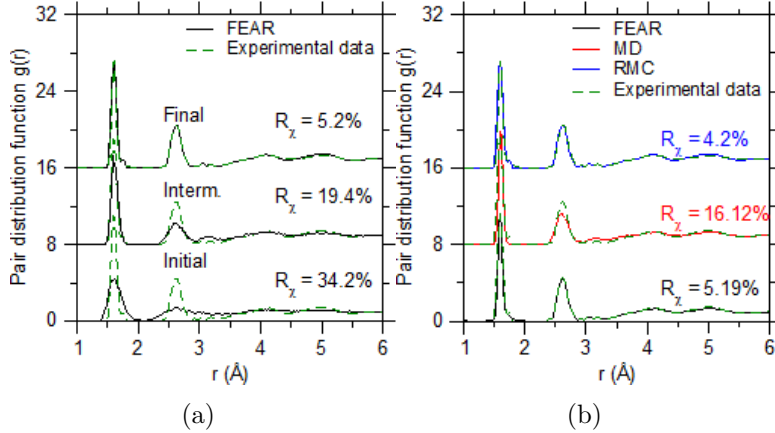
Figure 2.2: (a) Neutron pair distribution functions (PDFs) of the glassy silica structures formed by force-enhanced atomic refinement (FEAR) that are shown in Fig. 1. (b) Neutron PDFs of the final glassy silica structures generated by FEAR, molecular dynamics (MD, using a standard cooling rate of 1 K/ps), and reverse Monte Carlo (RMC). All the PDFs are compared with the same experimental neutron diffraction data 71.

After 20 FEAR iterations, we observe that the PDF of the final simulated configuration shows an excellent agreement with experimental neutron data, both for the short and medium-range length scales. As a measure of the level of agreement between simulations and experiments, we find that, at the end of the refinement, the Wright factor R_χ reaches a value of 5.2%. We note that this value is higher than the one that we previously obtained upon FEAR refinement of a sodium silicate glass 61, which highlights the unique challenges associated with the structure of glassy silica. Nevertheless, this final value is judged as satisfactory since R_χ values that are lower than 10% are typically considered to be indicative of a good agreement between simulations and experiments 73.

3.2. Comparison with molecular dynamics and reverse Monte Carlo

First, we compare the glass structure generated by FEAR with that offered by RMC. Figure 3a shows the evolution of the R_χ factor of the glass structure upon RMC refinement. We observe that the R_χ factor monotonically decreases and eventually reaches a final value of 4.2%, which is slightly lower than the value achieved by FEAR. This only indicates that RMC yields a pair distribution function that is in very good agreement with experimental neutron

16

diffraction data (see Fig. 2b). Such high level of agreement is not surprising since RMC refinement solely aims to decrease R_χ (i.e., R_χ is the only cost function during refinement). It is worth noting that, since they comprise energy minimization steps, FEAR simulations come with an additional computational burden as compared to traditional RMC. However, since the energy minimization is herein only performed every 3,000 RMC steps, the computational cost of FEAR simulations remains fairly dominated by the RMC steps. In practice, for a constant number of 20 (RMC or FEAR) iterations, a single simulation conducted on a single core of an Intel Xeon E5-2600 V2 processor is found to require 75h27 and 72h10 for FEAR and RMC, respectively—so that FEAR involves a 4.8% increase in computing cost. Nevertheless, we note that RMC requires slightly more iterations than FEAR to converge. This suggests that periodically minimizing the energy of the simulated structure (i.e., as done during FEAR refinement) effectively accelerates the refinement, that is, it decreases the number of RMC steps that are needed to achieve convergence—in line with previous findings.61 Overall, these results highlight the computational efficiency of the FEAR approach.

Figure 2b shows the neutron PDF of the glass structure generated by the melt-quench MD approach. We note that the PDF offered by MD only matches well with neutron diffraction data at low distance (i.e., for the first peak in the PDF), which indicates that MD offers a realistic description of the Si–O interatomic distance. Nevertheless, we find that, overall, MD yields a notably decreased level of agreement with experimental neutron diffraction data at larger distances (as compared to FEAR and RMC), which is illustrated by the larger value of the R_χ factor (16.1%, see Fig. 3b). The discrepancy between the experimental and MD-based PDFs mostly manifests itself in the second peak of the PDF, indicating that, in contrast with FEAR and RMC, MD partially misrepresents second-neighbor (O–O and Si–Si) correlations within the glass structure.

Next, we focus on the thermodynamic stability of the configuration generated by FEAR, RMC, and MD. Figure 3b shows the evolution of the molar potential energy of the system upon RMC refinement. Overall, we observe that RMC yields a potential energy that is

17

significantly higher than that offered by the other simulation approaches. Specifically, the molar potential energy of the structure generated by RMC is eventually about 360 kJ/mol larger than that of the structure simulated by MD. This is not surprising since RMC does not consider the interatomic energy of the system in its cost function. However, such high energy exemplifies the fact that, although the PDF calculated from the glass structure generated by RMC offers an excellent match with experimental neutron diffraction data, the configuration yielded by RMC is thermodynamically unstable. This echoes the fact the PDF is not a very discriminative metric to evaluate the soundness of a glass structure, that is, various structures featuring very different energies can nevertheless feature similar PDFs. Overall, these results indicate that, despite the apparent agreement with neutron diffraction data, RMC does not yield a realistic structure for glassy silica.

In contrast, Fig. 3b shows that FEAR eventually yields a potential energy that is significantly lower than that offered by both RMC and MD simulations. This is a key result since it implies that, although FEAR and MD rely on the same interatomic forcefield, the FEAR refinement scheme allows the simulated glass to reach more stable energy states. This arises from the fact that, during MD-based melt-quenching, the simulated glass quickly gets trapped within a given basin of the energy landscape as temperature decreases 76. The low value of the thermal activation then prevents the glass from escaping for this basin—so that the simulated glass retains a large fictive temperature (i.e., high-energy state). In contrast, upon FEAR refinement, the RMC steps that are performed in between each energy minimization tend to induce some slight structural perturbations that allow the simulated glass to overcome some large energy barriers that would be inaccessible during the limited timescale of MD simulations and, thereby, to reach deeper basins within the energy landscape. This establishes FEAR as a powerful method to generate simulated glass structures that are more stable than those created by MD. Overall, these results show that FEAR refinement can produce glass structures that simultaneously feature an unprecedented level of agreement with experimental neutron diffraction data and increased energetic stability.
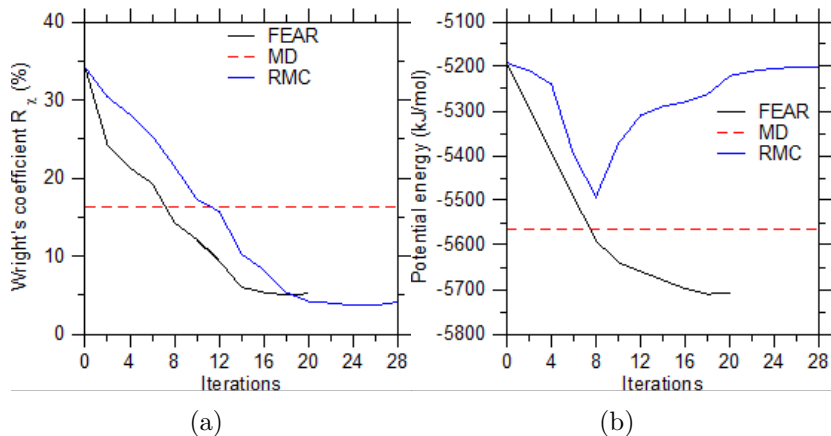
Figure 2.3: (a) Wright's coefficient R and (b) molar potential energy as a function of the number of iterations of force-enhanced atomic refinement (FEAR) and reverse Monte Carlo (RMC) refinement. Values obtained for a melt-quenched glass generated by molecular dynamics (MD) with a standard cooling rate of 1 K/ps are shown as horizontal dashed lines for comparison.

It is insightful to compare the differences in R_χ and potential energy yielded by the different simulation techniques considered herein with the level of variation that results from the use of different cooling rates in melt-quench MD simulations. To this end, Fig. 4a first shows the metric R_χ offered by MD simulations as a function of the cooling rate. As expected, R_χ decreases upon decreasing cooling rate. This indicates that, as the cooling rate decreases, the glass structure produced by MD gradually converges toward the experimental neutron diffraction data. On the other hand, independently of the cooling rate, the R_χ coefficient of the glass structures simulated by MD remains significantly higher than those obtained by RMC and FEAR refinement. In agreement with previous results 61, we find that the evolution of R_χ as a function of the cooling rate can be well described by a power law function—in line with mode-coupling theory 77. Using as a reference the power law relationship fitted based on the R_χ vs. cooling rate data obtained from MD (see Fig. 4a), we find, by extrapolation, that a cooling rate of about 10 K/s (i.e., 10-11 K/ps, vs. 10-2 K/ps for the longest MD simulation considered herein) would be needed for the MD simulation to yield an R_χ coefficient that is comparable to that offered by FEAR. Although this cooling

19
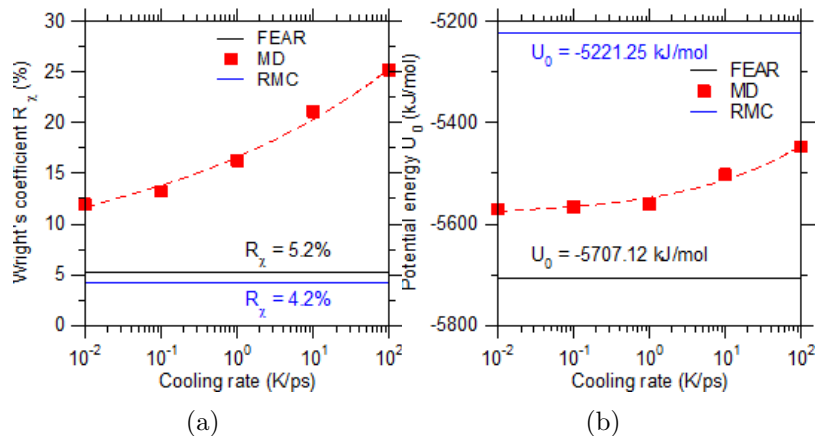
Figure 2.4: (a) Wright's coefficient R and (b) molar potential energy of melt-quenched glasses generated by molecular dynamics (MD) simulations as a function of the cooling rate. The dashed lines are some power law fits to guide the eye. Values obtained for the glasses generated by force-enhanced atomic refinement (FEAR) and reverse Monte Carlo (RMC) are shown as horizontal lines for comparison.

rate echoes typical experimental values, it is completely out-of-reach from MD simulations. These results highlight that the FEAR approach is able to generate atomic configurations that are comparable to well-annealed glass structures formed using slow cooling rates.

Figure 4b presents the evolution of the molar potential energy of the MD-simulated glasses as a function of the cooling rate. We observe that the potential energy decreases upon decreasing cooling rate. As expected, this implies that, as the cooling rate decreases, the system becomes more stable and be able to reach a deeper state within the energy landscape 76. Notably, even at the highest cooling rate (100 K/ps), the energy of the glass simulated by MD remains significantly lower than that of the RMC-based glass. This further illustrates the unrealistic nature of the glass generated by RMC. In contrast, we find that the energy of the glass generated by FEAR remains systematically lower than those of the glasses simulated by MD, even in the case of the slowest cooling rate (0.01 K/ps). This further confirms that FEAR yields a very stable glass structure that is associated with a low fictive temperature.

3.3 Effect of force-enhanced refinement on the short-range structure

20

In the following, we explore how the increased thermodynamic stability of the glass generated by FEAR is encoded in its structure. We first focus on the short-range order (<3.5 Å) structure. Figure 5 shows the Si–O, O–O, and Si–Si partial PDFs obtained by MD, RMC, and FEAR. We first observe that the first peak in the Si–O and O–O partial PDFs (around 1.6 and 2.6 Å, respectively) remains largely similar in the three simulated glasses. This indicates that FEAR refinement does not notably affect the average Si–O and O–O interatomic distances, which are already well predicted by MD and RMC (see Tab. 1). These average interatomic distances are in good agreement with available experimental data 78. In contrast, we find that, when compared with the MD-based glass, the Si–Si peak shifts toward higher distance upon FEAR refinement. This signals that, as compared to MD, FEAR predicts a higher average Si–Si interatomic distance, which exhibits an excellent match with experimental data (see Tab. 1) 78. Since the Si–O average distance remains constant, the increase in the Si–Si distance arises from an increase in the Si–O–Si angle (see below). In addition, the first Si–Si peak offered by FEAR is sharper than those predicted by MD and RMC. This indicates that FEAR yields a more pronounced degree of ordering between neighboring SiO4 tetrahedra than MD and RMC, which may explain the increased stability of the glass generated by FEAR.

Table 2.1: Average Si–O, O–O, and Si–Si interatomic distance values computed by force-enhanced atomic refinement (FEAR), molecular dynamics (MD), and reverse Monte Carlo (RMC) simulation. Experimental values sourced from Ref. 78 are provided for comparison.

	Si–O (Å)	O–O (Å)	Si–Si (Å)
Fear	1.611	2.624	3.067
MD	1.598	2.590	2.962
RMC	1.582	2.593	3.127
Experimental data	1.608 ± 0.004	2.626 ± 0.006	3.077

Then, we direct our attention to the short-range angular environment of each element. Figure 6 shows the O–Si–O (i.e., intratetrahedral) and Si–O–Si (i.e., intertetrahedral) PBADs offered by FEAR, RMC, and MD. We first note that the average O–Si–O angles predicted
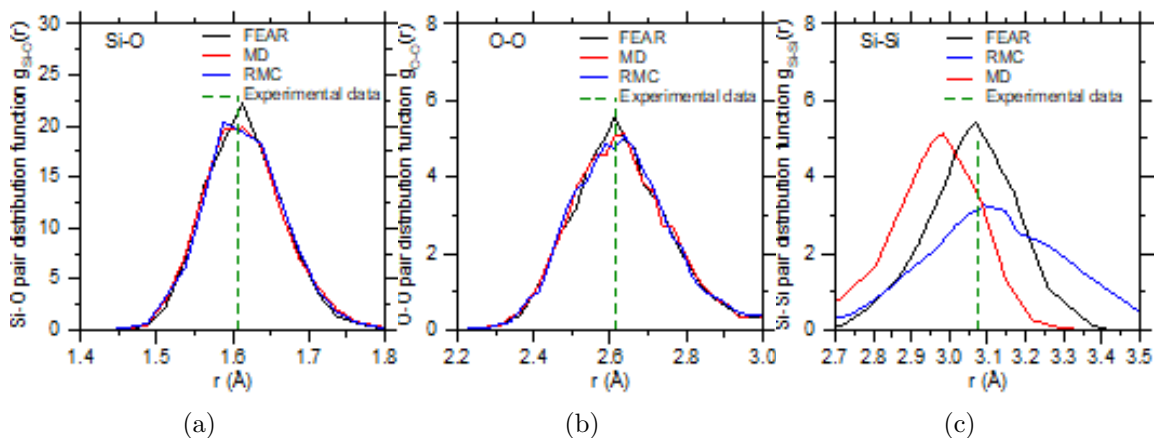
Figure 2.5: (a) Si–O, (b) O–O, and (c) Si–Si partial pair distribution functions computed by force-enhanced atomic refinement (FEAR), molecular dynamics (MD, using a cooling rate of 1 K/ps), and reverse Monte Carlo (RMC) simulation. The vertical dashed lines indicate experimental interatomic distances sourced from Ref. 78.

by these three simulation methods remain largely similar (around 109°). This value matches with available experimental data (see Tab. 2). This signals that the tetrahedral environment of Si atoms is already well-defined by MD and that FEAR does not induce any notable further refinements. However, we note that the O–Si–O PBAD becomes sharper upon FEAR refinement. This indicates that FEAR predicts a more ordered angular environment for Si atoms, while in turn, MD and RMC yield more distorted SiO4 tetrahedral. This echoes the fact that, based on previous MD results, the O–Si–O PBAD tends to become sharper upon decreasing cooling rate, that is, as the glass becomes more stable 13.

We then focus on the Si–O–Si PBAD. We find that the Si–O–Si PBAD offered by FEAR exhibits a notable shift as compared to MD and RMC data. The average Si–O–Si angle predicted by FEAR is significantly larger than that predicted by MD. The opening of the Si–O–Si angle predicted by FEAR is in agreement with the larger Si–Si distance observed in Fig. 5c and is well supported by available experimental data 71,79–83 The shift of the Si–O–Si angle toward larger values also echoes the fact that, based on previous MD results, this angle tends to increase upon decreasing cooling rate, that is, as the glass reaches lower fictive temperatures 13. We also note that FEAR yields a sharper Si–O–Si PBAD than MD,

22
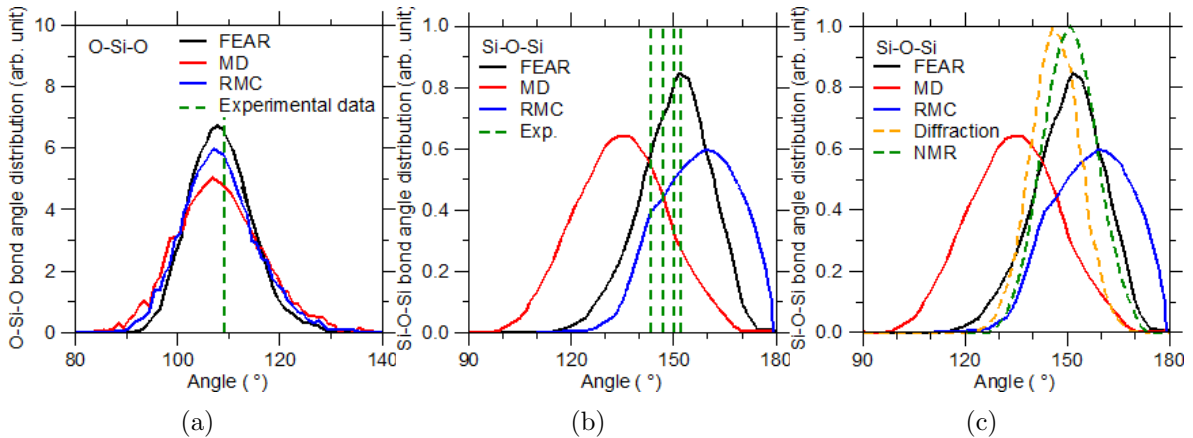
Figure 2.6: (a) O–Si–O and (b) Si–O–Si partial bond angle distributions computed by force-enhanced atomic refinement (FEAR), molecular dynamics (MD, using a standard cooling rate of 1 K/ps), and reverse Monte Carlo (RMC) simulation. The vertical dashed lines indicate experimental average angle values obtained from different experimental data 80–84 (c) Si–O–Si partial bond angle distributions computed by FEAR, MD, and RMC simulation, which are compared with reference PBADs computed from combined neutron and photon diffraction 79 and nuclear magnetic resonance (NMR) experimental data 81

which, once again, matches with the fact that, based on previous MD results, this PBAD tends to sharpen upon decreasing cooling rate 13. This is also in agreement with the sharp PBAD that was inferred from experimental nuclear magnetic resonance (NMR) data in Ref. 83 (see Fig. 6c). This sharpening of the Si–O–Si PBAD indicates that FEAR predicts an increased degree of ordering in between neighboring SiO4 tetrahedra compared to MD and RMC. Overall, the distinctive features of the short-range order of the glass yielded by FEAR are all supported by experimental data and offer a structural basis for the increased thermodynamic stability of the glass generated by FEAR.

3.4 Effect of force-enhanced refinement on the medium-range structure

Finally, we explore how the increased thermodynamic stability of the glass generated by FEAR manifests itself in its medium-range order structure of the simulated glass structure. To this end, we compute the neutron structure factor for each of the simulated glasses (see Sec. 2.6). Figure 7 shows the reduced structure factor predicted by FEAR, RMC, and MD, which are compared with neutron diffraction data 71. We first observe that all the

Table 2.2: Average interatomic angle values computed by force-enhanced atomic refinement (FEAR), molecular dynamics (MD, using a cooling rate of 1 K/ps), and reverse Monte Carlo (RMC) simulation. Computed data are compared with experimental values sourced from Refs. 79–83, which are based on X-ray diffraction (XRD), high-energy X-ray diffraction (HXRD), and 29Si Nuclear magnetic resonance (NMR) spectroscopy data. The full-width at half-maximum (FWHM) of the Si–O–Si partial bond-angle distribution is also indicated for.

	O–Si–O	Si–O–Si	FWHM of Si–O–Si
Fear	109.2°	152.9°	23.4°
MD	107.6°	137.4°	31.8°
RMC	108.6°	161.6°	34.2°
Combined			
neutron and	109.47°	148.3°	17.2°
photon diffraction[79]			
²⁹Si NMR[80]	109.47°	150.1°	21.4°
²⁹Si NMR[81]	109.7°	151°	18.7°
HXRD[82]	109.3°	147°	35.5°
Combined			
neutron and x-ray[83]	109.47°	141°	22.1°

simulation techniques considered herein (MD, RMC, and FEAR) offer a realistic prediction of the glass structure factor, since the positions of the peaks are well reproduced (see Fig. 7a). Especially, the structure factors predicted by all these techniques exhibit a good match with experimental data in the high-Q domain, which echoes the fact MD, RMC, and FEAR all offer a fairly realistic description of the short-range order structure of the glass. On the other hand, we observe the existence of some discrepancies in the low-Q region between the structure factor predicted by MD and experimental data (see Fig. 7b). In particular, the intensity and degree of asymmetry of the first-sharp diffraction peak (FSDP) around 1.5 Å 1 is not well predicted by MD. This suggests that MD offers a poor description of the medium-range order structure of the glass. In contrast, we find that both RMC and FEAR refinements offer a significantly improved description of the low-Q region of the structure factor. Importantly, the intensity, position, and the degree of asymmetry of the FSDP are well-reproduced by RMC and FEAR. This suggests that, although the level of structural

refinement enabled by FEAR (and RMC) does alter the Si–O–Si angular distribution (see Fig. 6c), the refinement primarily affects the medium-range order structure of the simulated glass. Specifically, the fact that FEAR predicts a sharper FSDP than MD suggests that the glass refined using FEAR exhibits a more ordered medium-range structure than its MD-based counterpart—which is the main structural feature that may explain the increased stability (i.e., lower energy) of the FEAR-based glass.

In glassy silica, the medium-range order is primarily encoded in the ring size distribution, wherein silicate rings are defined as the shortest closed paths made of Si–O bonds within the atomic network 10,74. To further explore how the enhanced thermodynamic stability enabled by FEAR refinement finds its origin in the medium-range order of the glass structure, we compute the ring size distribution of each model by using the RINGS package 74 while using the Guttman's definition for the rings' calculation (see Sec. 2.6).

Figure 8a presents the ring size distribution computed by FEAR, RMC, and MD simulations. We note that the ring size distribution predicted by MD is in good agreement with previous works 14,48,71,85, being centered around 5-to-6-membered rings—wherein the ring size is expressed in terms of the number of Si atoms it comprises. However, we observe some differences between the ring size distributions predicted by MD, RMC, and FEAR. Notably, we observe that FEAR yields a sharper ring size distribution than that predicted by MD, which, once again, highlights the fact that the glass generated by FEAR exhibits a more ordered medium-range order structure than its MD counterpart. This result echoes previous findings obtained for a sodium silicate glass 61. The sharpening of the ring size distribution observed herein is also in agreement with recent MD results, which showed that the ring size distribution tends to become sharper upon decreasing cooling rate, that is, as the glass becomes more stable 45.

Although no direct measurement of the ring size distribution is available to date to validate the computed ring size distributions for 3D silica glass 86, these results can be compared with the outcomes of the RingFSDP approach introduced by Shi et al. 42,87. In brief, this
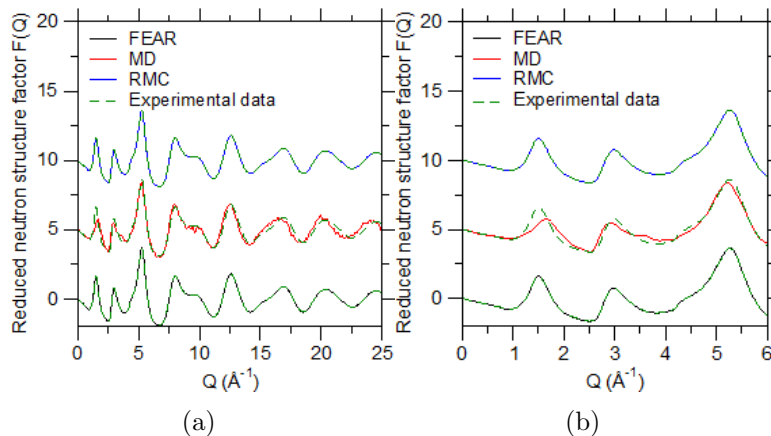
Figure 2.7: (a) Reduced neutron structure factor of the glassy silica structures generated by force-enhanced atomic refinement (FEAR), molecular dynamics (MD, using a cooling rate of 1 K/ps), and reverse Monte Carlo (RMC) simulation. The data are compared with the same experimental neutron diffraction data 71. Panel (b) shows a zoom of the low-Q domain of the same structure factors.

method consists in deconvoluting the FSDP of the structure factor into the contribution of three types of rings: small (4-membered and smaller), intermediate (5-membered), and large (6-membered and larger)—which makes it possible to estimate the fraction of these three families of ring. Figure 8b shows the computed fractions of small, intermediate, and large rings predicted by MD, RMC, and FEAR. When compared with MD results, we find that FEAR refinement results in (i) a decrease in the fraction of small rings and (ii) an increase in the fraction of large rings. Both of these behaviors are well supported by the outcomes of the RingFSDP analysis 71. This confirms that FEAR yields a realistic description of the medium-range order structure of glassy silica.

The fact that FEAR predicts a lower fraction of small rings echoes the fact that such small rings, due to their topologically-over constrained nature, have been noted to be unstable due to the existence of small atomic-level internal stress 45. Hence, small rings tend to disappear as the glass relaxes toward lower energy states 45. This disappearance of small rings resulting from FEAR refinement (as compared to MD) is also in agreement with the increase in the average Si–O–Si angle observed in Fig. 6b. Indeed, it has been reported that small rings
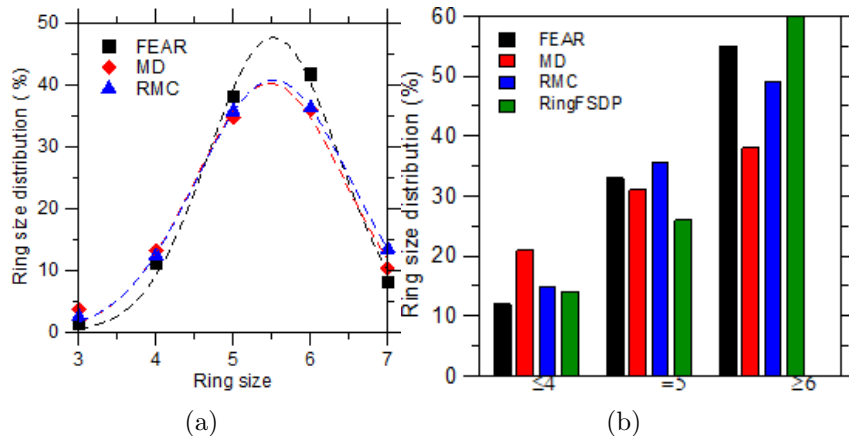
Figure 2.8: (a) Ring size distribution of the glassy silica structures generated by force-enhanced atomic refinement (FEAR), molecular dynamics (MD, using a cooling rate of 1 K/ps), and reverse Monte Carlo (RMC) simulation. The dashed lines are to guide the eye. (b) Computed fractions of small ($\leq$ 4-membered), intermediate (5-membered), and large ($\geq$ 6-membered) rings in the glassy silica structures generated by FEAR, MD, and RMC. The data are compared with reference data inferred from diffraction data using the RingFSDP method 71.

are associated with strained, smaller Si–O–Si angle, which is another signature of the fact that small rings are experiencing some internal stress. Overall, these results suggest that the stable nature of the glasses generated by FEAR largely arises from the fact that such glasses exhibit a more ordered medium-range order structure featuring fewer unstable small rings.

4. Discussion

Finally, we discuss to which extent the outcome of FEAR refinement depends on the used interatomic forcefield. This is an important question since, for instance, the structure of glasses simulated by MD simulations strongly depends on the details of the interatomic potential that is used 5. To this end, Fig. 9a-e shows the pair distribution function, reduced neutron structure factor, bond angle distributions, and ring size distribution predicted by FEAR while using three distinct interatomic potentials (see Methods section). Overall, we find that all these potentials yield virtually the same pair distribution function, neutron

structure factor, bond angle distribution and, importantly, the same ring size distribution. This contrasts with the case of MD simulations, wherein the forcefield has a direct and significant impact on the simulated structure. Specifically, in MD simulations, the Si–O–Si partial bond angle and ring size distributions are often very sensitive to the choice of the interatomic forcefield. The fact that the outcome of the FEAR simulation does not notably depend on the choice of the interatomic potential can be understood from the fact that, in FEAR, the structure is mostly determined by the RMC steps, but only weakly impacted by the energy minimization. Rather, here, the energy minimizations solely ensure that the structure never deviates too much from an energetically stable state upon RMC refinement. Overall, in the FEAR approach, the role of the interatomic potential is only to discriminate stable from unstable structures generated by RMC, which effectively mitigates the ill-defined nature of RMC refinement. This suggests that FEAR simulations are not largely sensitive to the choice of the interatomic potential that is used and that, in contrast to MD simulations, even a poorly parameterized forcefield might yield realistic results when used within the FEAR approach.
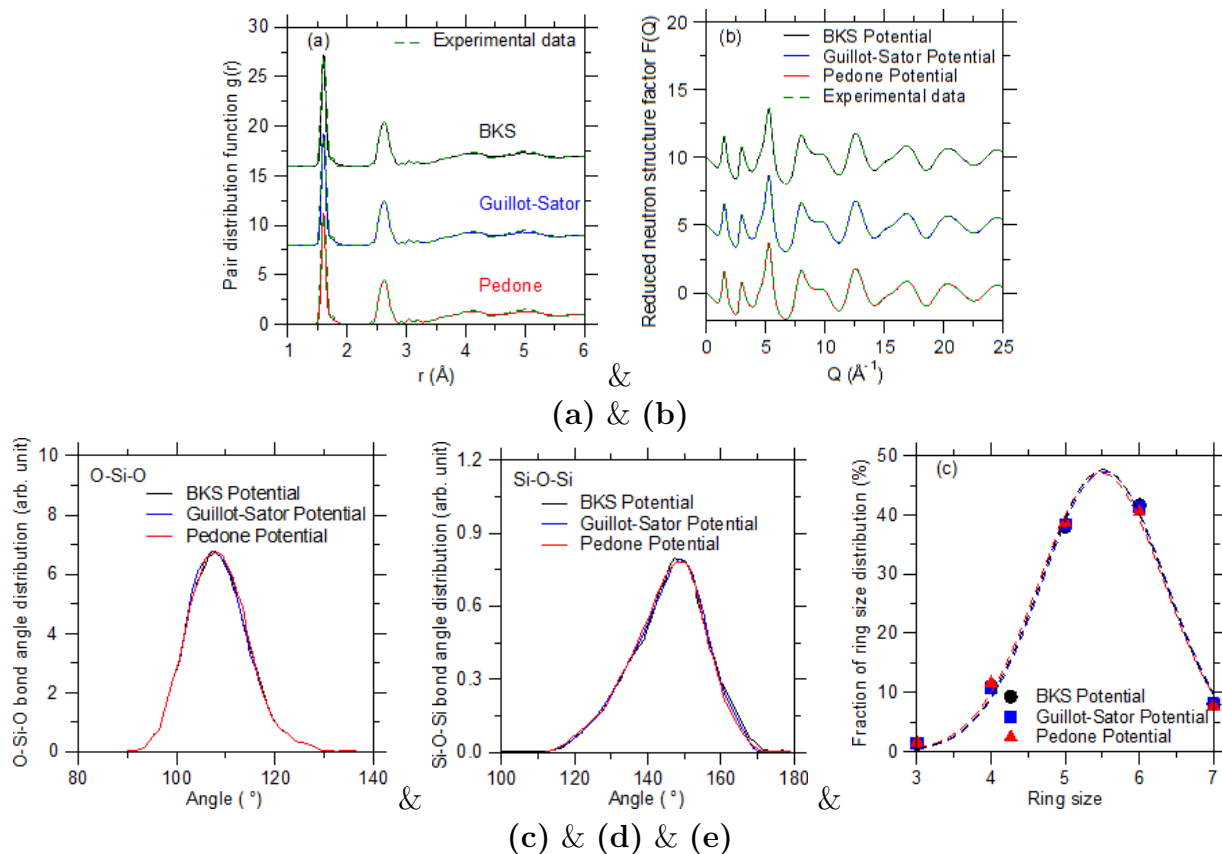
Figure 2.9: Comparison of the **(a)** pair distribution function, **(b)** reduced neutron structure factor F(Q), **(c)** O–Si–O, **(d)** Si–O–Si partial bond angle distributions and **(e)** ring size distribution computed by FEAR while using different interatomic potentials. The structure factors are compared with the same experimental from neutron diffraction data 71.

5. Conclusions

All these results demonstrate that FEAR offers an improved description of the atomic structure of glassy silica as compared to traditional MD simulations based on the melt-quench method or RMC simulations. This is evident from the fact that FEAR yields a glass that simultaneously exhibits enhanced agreement with available experimental data and increased energetic stability. Overall, we find that the increased stability enabled by FEAR primarily arises from the fact that the generated glass exhibits a more ordered medium-range order structure and a lower fraction of unstable small silicate rings, which, in turn, tends to induce an opening of the Si–O–Si inter-tetrahedral angle. These results establish FEAR as a

promising technique to "invert" available experimental into realistic, stable glass structures and to overcome the intrinsic limitations of traditional MD simulations. Importantly, unlike MD simulations, FEAR simulations are not very sensitive to the details of the interatomic potential that is used. This suggests that FEAR could be used to simulate a wide array of glass families, even in the absence of a robust interatomic forcefield. Overall, this approach could leapfrog one's ability to reveal the hidden atomic structure of complex disordered materials.

CHAPTER 3

Origin of the Anomalous Low Thermal Expansion of Glassy silica

Upon a change in temperature, non-crystalline solids exhibit some variation in their volume—which is captured by their coefficient of thermal expansion. In that regard, glassy silica—an archetypical oxide glass—exhibits an anomalously low bulk thermal expansion, which is more than an order of magnitude lower than the thermal expansion of the interatomic bonds within its atomic network. Here, by combining in-situ neutron diffraction experiments and force-enhanced atomic refinement simulations, we investigate the effect of temperature on the atomic structure of glassy silica at various scales. We reveal that the low thermal expansion of glassy silica is governed by a compaction of the shape of the silicate rings in the medium-range order, which counterbalances the interatomic expansion in the short-range order.

The coefficient of thermal expansion (CTE) captures the rate at which a phase expands upon an increase in temperature. In particular, the thermal expansion of glasses is a phenomenon that can induce thermal cracking or undesirable length variations in display substrates. In contrast to crystalline solids, non-crystalline phases tend to exhibit more complex responses upon varying temperature 88. In that regard, the thermal expansion of glassy silica (SiO2, an archetypical system that silicate glasses are based on) is unique in many ways. Indeed, glassy silica features an unusually low linear CTE of 0.55×10^{-6} K^{-1}, which is the lowest out of those of all the major glass-forming binary oxides 88, including glassy germania (GeO2, 7.48×10^{-6} K^{-1}) 89. The CTE of glassy silica is also more than one order of

magnitude lower than those its isochemical crystalline phases, including -cristobalite (10.9 × 10^6 K^{-1}) and α-quartz (15×10^6 K^1).

The origin of the low CTE of glassy silica is necessarily structural—since, from a microscopic viewpoint, thermal expansion is encoded in the response of the atomic structure to temperature variations. At the atomic level, the thermal expansion of solids typically first originates from the asymmetry of the interatomic potential energy, which results in an elongation of the interatomic bonds upon increasing temperature. However, the bulk linear CTE of glassy silica is surprisingly more than one order of magnitude lower than that of the Si–O interatomic bonds (9.1 × 10^{-6} K^{-1}, see Fig. 1a) 71, which suggests that the expansion of the interatomic bonds is counterbalanced by the shrinkage of larger-scale structural features. At the scale of the polytopes, the CTE of SiO2 polymorphs is also impacted by the amplitude of the rigid unit modes, that is, the variations within the mutual orientation of neighboring SiO4 polytopes, as captured by the Si–O–Si intertetrahedral angle. Identifying the origin of the discrepancy between microscopic and bulk thermal expansion is further complicated by the fact that, as an out-of-equilibrium phase, glassy silica's properties depend on its thermal history—although the effect of thermal history on silica's CTE is limited to about ±20% variations. Altogether, no clear structural mechanism has thus far been proposed to offer a self-consistent, quantitative explanation of the low CTE of glassy silica.

In this Letter, we combine in-situ neutron diffraction experiments and force-enhanced atomic refinement (FEAR) simulations to explore how temperature is affecting the atomic structure of glassy silica at several scales (from the short- to the medium-range order). We reveal that, ultimately, the answer to this question lies in the shape of the silicate rings in the medium-range order, which, by becoming more elliptic upon increasing temperature, tend to become more compact—thereby counterbalancing the expansion of the interatomic bonds.

To establish our conclusions, we first rely on time-of-flight (TOF) neutron-scattering measurements of fused silica 7940 samples performed from room temperature to 950℃. More

detail on these measurements can be found in Supplementary Material and in Ref. 71. These experiments allow us to extract the neutron structure factor and pair distribution function of glassy silica under varying temperature. By following the methodology described in Ref. 71, we then extract the Si–O and O–O interatomic distances as a function of temperature by fitting the peaks of the structure factor by some Gaussian distributions (see Ref. 71 for details). As mentioned before and shown in Fig. 1a, the rate at which the Si–O interatomic bonds expands upon increasing temperature (as captured by the relative increase, or strain) far exceeds that of the bulk volumetric expansion of glassy silica—which highlights an intriguing mismatch the short-range and bulk thermal expansion.

Since glassy silica does not exhibit any long-range order, we then turn our attention to the medium-range order. To this end, we track the temperature-dependence of the first-sharp diffraction peak (FSDP) in the neutron structure factor, which captures the spatial frequency of typical repetition distances in the medium-range order. Using the RingFSDP method 90,91, we convert the FSDP into a real-space medium-range order distance by fitting the FSDP by a series of Gaussian distributions (see Ref. 71 for details). As shown in Fig. 1a, the rate at which the medium-range order distance expands upon increasing temperature also far exceeds that of the bulk volumetric expansion of glassy silica (as well as that of the Si–O bonds). This indicates that the origin of the low CTE of glassy-silica is subtle and might not be directly encoded in two-point correlation functions like the structure factor or the pair distribution function.

Since one-dimensional two-point-projection signatures of the atomic structure are insufficient to resolve the origin of the CTE of glassy silica, we then turn to the analysis of the three-dimensional atomic structure itself—which, to date, can only be accessed by atomistic simulations. However, conventional molecular dynamics (MD) simulations of silicate glasses are plagued by the use of extremely high quenching rates (typically, 1 K/ps), which far exceed that used in experiments (typically 1 K/s) 92,93. As a result, glass structures generated by MD tend to be more disordered than that of experimental glasses and, rather,

33

tend to mimic that of hyperquenched glasses. To overcome this challenge, we adopt the force-enhanced atomic refinement (FEAR) technique—a powerful modeling approach that efficiently combines several iterations of reverse Monte Carlo (RMC) refinements and energy minimizations to generate glass structures that simultaneously exhibit good agreement with experimental data and thermodynamic stability 94.

In detail, we generate SiO2 structures made of 3,000 atoms at varying temperatures. Using the FEAR approach described in Ref. 95, we "invert" the pair distribution functions of glassy silica obtained herein by neutron diffraction under varying temperatures into three-dimensional structures. To ensure thermodynamic stability and address the ill-defined nature of RMC, the energy generated structures are periodically minimized based on the well-established BKS forcefield 96. We previously showed that this approach yields SiO2 glasses that simultaneously exhibit an excellent match with neutron diffraction data (notably improved as compared to MD simulations) and an extremely high thermodynamic stability (wherein the simulated structures reach an internal energy that is well below that that can be achieved by melt-quenching MD simulations) 95. Here, we find that that the same level of agreement with diffraction data and thermodynamic stability is maintained for glasses associated with varying temperatures (see Supplementary Material). Note that, here, the effect of temperature is solely encoded in the temperature-dependent diffraction data used as input for the RMC refinements.

Altogether, the FEAR approach yields a series of realistic three-dimensional glass structures associated with varying temperatures that we can use as a basis to seek for the structural origin of the low thermal expansion. To this end, we analyze the generate structures at various scales, starting with the short-range order. We first find that the computed thermal expansion of the Si–O and O–O interatomic distances exhibit a good match with the neutron diffraction data obtained herein (see Fig. 1b). Although this is not surprising since the diffraction data are used as input for the FEAR simulation, this confirms that the simulated structures are realistic and that interatomic distances expand significantly more than the
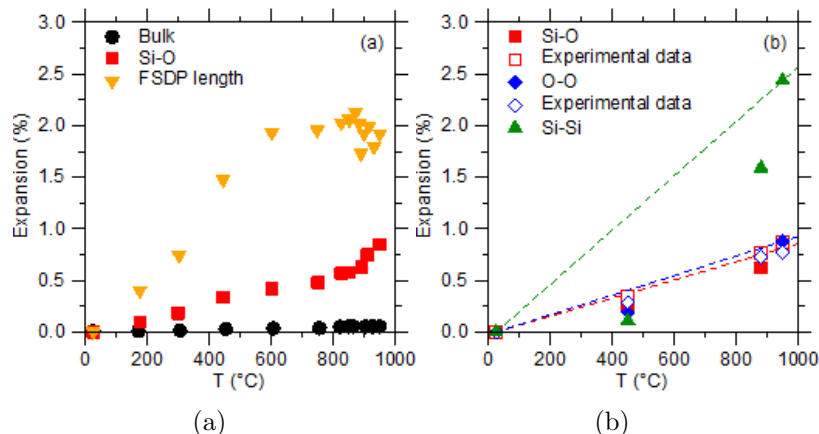
Figure 3.1: (a) Relative expansion of the bulk volume, Si–O interatomic distance, and medium-range order distance inferred from neutron diffraction as a function of temperature 71. (b) Relative expansion of the Si¬–O, O¬–O, and Si–Si interatomic distances computed by FEAR as a function of temperature. The computed data are compared with experimental data at the same temperatures 71.

bulk glass volume upon increasing temperature. In addition, the simulated structures allow us to compute the Si–Si interatomic distance, which is otherwise "invisible" from neutron diffraction. We observe that the thermal expansion of the Si–Si interatomic distance is notably larger than that of the Si–O or O–O bonds (see Fig. 1b)—in agreement with previous simulation. Note that, in contrast the Si–O and O–O, the expansion of the Si–Si distance is non-linear with temperature. This expansion indicates that, in addition to the elongation of the Si–O bonds, glassy silica also features an increase the intertetrahedral Si–O–Si angle upon increasing temperature. The opening of the Si–O–Si angle further enhance the thermal expansion of the short-range order of glassy silica and hence, further increases the mismatch between short-range and bulk thermal expansion.

Having confirmed the mismatch between short-range and bulk thermal expansion, we now revisit the role of the medium-range order. In that regard, the three-dimensional atomic structures generated by FEAR allow us to directly access the medium-range order structure of glassy silica and its temperature dependence. Indeed, although neutron diffraction only offers a "signature" of the medium-range order (i.e., the FSDP), the FEAR can be used to

describe the topology of the silicate rings forming within the atomic network—wherein the rings are defined as the shortest closed paths made of Si–O bonds within the network. In line with previous simulation, we observe that the silicate rings show an average size of around 5-to-6 (see Supplemental Material).

Next, based on the atomic structure generated by FEAR, we explore how the topology of the silicate rings depends on temperature. We first note that the size of the rings (as measured in terms of the number of Si atoms they are made of) does not notably change with temperature. This is not surprising since all the temperatures considered herein are lower than the glass transition temperature so that the network connectivity is expected to remain largely frozen. As such, the average perimeter of the ring rapidly expands upon increasing temperature since it is proportional to the Si–Si interatomic distance (see Supplemental Material). Using a circular assumption, the perimeter length P can be converted into an effective radius R following P= 2R. As shown in Fig. 3a, the thermal expansion of this effective ring radius is notably higher than the bulk volumetric expansion of glassy silica, which indicates that the size of the rings (as captured by their perimeter or effective radius) is unable to explain the low CTE of glassy silica. Interestingly, we find that the relative expansion of the effective radius of the rings matches that of the medium-range distance inferred from the FSDP (see 1a), in agreement with the fact that the FSDP captures the spatial frequency of the typical repetitions' distances in the medium-range order (i.e., the rings effective radius). This confirms that the low CTE of glass silica cannot be understood from simple 2-point correlation analyses implicitly assuming that the atomic structure is isotropic and that the silicate rings are circular.

To go beyond these assumptions, we further describe the topology of the silicate rings by computing their effective area A. To this end, we first describe each ring based on the coordinates of the Si atoms it is made of. This allows us to calculate the centroid of each ring, as the geometric average of the position of the Si atoms. Next, to capture the ring shape, we fit each ring by an ellipse centered around its centroid—wherein the major and

minor radii a and b of the ellipse are optimized by gradient descent to minimize the mean squared distance between the Si atoms and the ellipse (see schematic in Fig. 2a). This analysis allows us to calculate the effective area A of each ring as A= ab. Note that, for most of the rings (from 4-to-7 membered rings), no significant deviation from planarity is observed so that we restrict our analysis to being two-dimensional.

Figure 3a shows the computed ring effective area A as a function of the effective radius R, as averaged over distinct ring size (i.e., 4, 5, 6, and 7-membered rings). As expected, both the radius and area of the rings increases with their size (from 4-to-7 membered rings). Data are also shown for varying increasing temperatures (from room-temperature to 950°C), wherein lighter colors indicate higher temperatures (see Fig. 3a). As expected, the effective radius of the rings increases with temperature, irrespectively of the ring size. To appreciate how temperature affects the area of the rings, Fig. 3a first shows what would be the effective area of the rings if they were perfectly circular, that is, assuming that the area is given by A= R^2 (see the dashed line in Fig. 3a). Importantly, we note that the computed effective areas of the rings (by fitting them by ellipses) are notably lower than those expected if the rings were circular. This indicates that the shape (i.e., ellipticity) of the rings plays a significant role in defining how much space they occupy within the atomic network. Importantly, we note that the degree of ellipticity (as defined from the deviation from circularity) increases upon increasing temperature, irrespectively of the ring size (see Fig. 3a). The effect of ellipticity is especially pronounced for the smallest rings (i.e., 4-membered rings), for which the increase in the degree of ellipticity upon increasing temperature is so large that their average effective area eventually decreases with temperature (despite the increase of their average effective radius). This is likely a consequence of the fact that such small rings are topologically overconstrained and, as a result, experience some internal stress 15, which, in turn, promotes relaxation upon heating 97.

Next, based on the computed effective areas of each ring, we calculate the average ring area (averaged over all the ring sizes). Figure 2b shows the evolution of the average ring

37
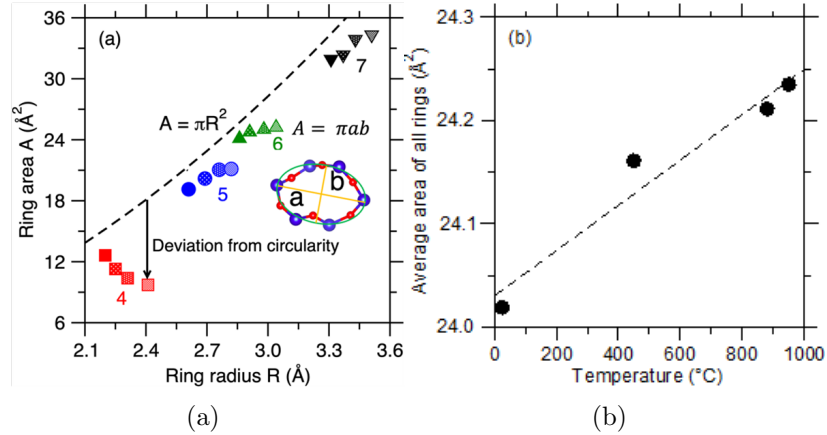
Figure 3.2: (a) Effective ring area A computed by FEAR as a function of the effective ring radius R (see text). The area and radius values are averaged over groups of ring sizes (i.e., 4, 5, 6, and 7-membered rings). Data are showed for varying increasing temperatures, wherein lighter colors indicate higher temperatures. The dashed line indicates the area that would be expected if the rings were circular. The schematic illustrates how the rings are fitted by ellipses, wherein Si and O atoms are indicated in blue and red, respectively. (b)Average effective ring area (averaged over all the ring sizes) computed by FEAR as a function of temperature. The dashed line is a linear fit.

area as a function of temperature. Since the degree of planarity of the rings does not notably change upon varying temperature, we use the temperature-dependence of the average ring area to define the relative expansion of the silicate rings. Figure 3a shows the relative expansion of various structural features associated with varying scales (namely, in order of increasing scale, Si–O, O–O, and Si–Si interatomic distance, ring effective radius, and ring effective area). The data are compared with the bulk volumetric relative expansion of glassy silica (black symbols in Fig. 3a) that is used to define its bulk CTE. All these data are then used to calculate the CTE values associated with each of these structural features, which are summarized in Fig. 3b. Note that the surface CTE obtained from the ring area is converted into a linear CTE before being plotted in Fig. 3b to ensure a consistent comparison. These results highlight that the CTE associated with the ring area exhibit a very close match with the bulk CTE of glassy silica. This indicates that the macroscopic thermal expansion of glassy silica is quantitively encoded in the shape of the silicate rings.

38
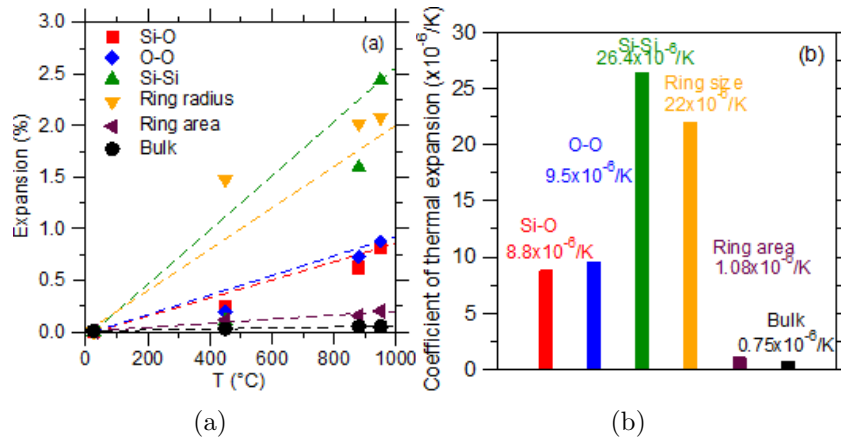
Figure 3.3: (a) Relative expansion of the Si–O, O–O, and Si–Si interatomic distances, average effective ring radius, and average effective ring area computed by FEAR as a function of temperature. The data are compared with the macroscopic bulk volumetric expansion of glassy silica. The dashes lines are linear fits. (b) Linear coefficient of thermal expansion associated with all the structural features considered in panel (a).

Overall, Fig. 3b offers a self-consistent and quantitative description of the thermal expansion of each structural feature of glassy silica, and how the distinct effects of these features eventually accumulate and culminate into governing the macroscopic thermal expansion of glassy silica. The following atomic picture emerges from these results. As temperature increases, both the interatomic distances and angles increases, which results in a large expansion of the short-range order. However, this short-range order expansion is eventually compensated by the fact that the silicate rings become more elliptic upon increasing temperature and, hence, become more compact (since the area of an ellipse is lower than that of a circle at constant perimeter). The competition between short-range expansion and medium-range compaction eventually explains the very small CTE featured by glassy silica. In that regard, it is worth noting that the area of the rings does not compensate the expansion of the Si–O bonds; rather, the ring area capture the culminating and combined effects of the interatomic bonds, angles, and ring shape—so that the CTE associated with the average ring area can indeed directly and quantitatively be compared the bulk CTE of glassy silica.

Overall, besides unveiling the atomic origin of the low CTE of glassy silica, these results

39

highlight the important role of the shape (i.e., ellipticity and, potentially, planarity) of the silicate rings and, more generally, of anisotropy in the structure of glasses. Such complex topological information cannot easily be extracted from experimental data—which typically only offer two-point projections as indirect signatures of the three-dimensional atomic structure of glasses—and can only be accessed by advanced modeling techniques like FEAR. These results also highlight the special roles played by small rings, which, on account of their topologically-overconstrained nature, tend to behave differently than larger, topologically flexible rings. This suggests that tuning the size and shape of rings (e.g., via varying thermal or pressure treatments or via the inclusion of network modifiers) offers an important degree of freedom to discover new glasses with tailored properties.

CHAPTER 4

Experimental Method to Quantify the Ring Size Distribution in Silicate Glasses and Simulation Validation Thereof

In contrast to their crystalline counterparts, glasses lack any long-range order. In turn, for energetical reasons, glasses often exhibit a short-range order that is fairly similar to that of crystals [1]. As such, the distinctive out-of-equilibrium nature of the glassy state is largely associated with the uniqueness of glasses' medium-range order. The existence of some level of order in the medium-range structure of oxide and chalcogenide glasses is often linked with the onset of a first-sharp diffraction peak (FSDP) in their diffraction pattern—which denotes that some well-defined structural units associated with intermediate typical repetition distances can be found in the structure of glasses [2]. In silicate glasses, the medium-range order structure is primarily encoded in the ring size statistics—wherein a ring is defined as a closed-path in the atomic network of glasses. Although the ring statistics play a key role in governing glass properties [3], this structural feature is largely invisible to conventional experimental techniques and, hence, remains mostly unknown.

As an alternative route to experiments, atomistic simulations can infer the structure of a glass based on some available information (e.g., the interatomic forcefields) and, hence, provide direct access to the ring statistics in simulated glasses [4] [5]. However, such modeling techniques are affected by their own limitations [6]. On the one hand, molecular dynamics (MD) simulations leverage the knowledge of interatomic forcefields to form glasses by "melt-

quench," but are plagued by the need to use high cooling rates. This raises questions about their ability to offer a realistic description of glasses' medium-range order—especially since the ring statistics strongly depends on the cooling rate [7]. On the other hand, reverse Monte Carlo (RMC) simulations are used to invert available experimental data into a three-dimensional structure, but RMC-based structures are often thermodynamically unstable [8]. More generally, constructing realistic atomic structures for glasses that match available experimental signatures (e.g., diffraction patterns) is intrinsically an ill-defined problem since an infinite number of atomic structures can yield the same signatures. As such, although it is straightforward to determine that a model glass structure is invalid (if it does not match with at least one experimental signature), it is virtually impossible to robustly demonstrate that a model glass structure is valid. All these aspects demonstrate the difficulties associated with the fact of revealing the true medium-range order structure of glasses.

To uncover glasses' medium-range order, we developed a heuristic method (RingFSDP) that, based on experimental data, aims to extract the ring size distribution in a silicate glass from the shape of its neutron structure factor's FSDP (FFSDP(Q)) [9]. In this method, the FSDP is deconvoluted into three Gaussian distributions with fixed average reciprocal lengths Q, wherein each distribution is ascribed to a certain family of rings: (i) large rings ($\geq$ 6-membered) centered at low Q, (ii) medium rings (5-membered) centered at intermediate Q, and (iii) small rings ($\leq$ 4-membered) centered at large Q. Note that the ring sizes are here expressed in terms of the number of network-forming atoms they are made of. The fraction of each of these three types of rings is then determined from the relative integrated area under each of these three Gaussian distributions. However, like any empirical methods developed from experimental data, the model-free RingFSDP approach relies on two core assumptions regarding how each type of ring contributes to the FSDP: (i) FFSDP(Q) is comprised of three Gaussian distributions Fn(Q) that are associated with different groups of ring sizes and (ii) the average position of these Gaussian distributions is fixed and does not depend on the glass composition (e.g., the identity of glass former species comprising the

ring, namely, Al and Si in aluminosilicate glasses). In this contribution, we validate these two assumptions, which offers a robust, sound foundation for the RingFSDP method.

Here, to establish our conclusions, we first uncover by simulation the valid structure of two representative silicate glasses by combining neutron diffraction experiments and force-enhanced atomic refinement (FEAR) [8] [10] [11]. We then compute the ring size distribution from the FEAR-simulated structures and isolate the contribution of each ring size to the structure factor FSDP. Based on these results, we offer a robust support for the two core assumptions of the RingFSDP method. Eventually, we demonstrate that the ring size distribution in silicate glasses can indeed be experimentally determined based on the deconvolution of their FSDP.

Results

Uncovering glass structure by FEAR simulations

To establish our conclusions, we investigate the medium-range order of two representative silicate glasses, namely, glassy silica and an industrial alkaline-earth aluminosilicate glass named Jade® [12]. These two glasses are chosen so as to ensure that the method developed herein applies to the archetypical SiO2 glass, as well as a more complex modified silicate glass Jade®—(CaO)6(MgO)7(Al2O3)13(SiO2)74—which comprises some network modifiers and two network-forming elements. The atomic structure of these two glasses is investigated at room temperature by performing time-of-flight (TOF) neutron scattering measurements on the Nanoscale-Ordered Materials Diffractometer (NOMAD) at the Spallation Neutron Source (SNS), Oak Ridge National Laboratory (see Methods section). This yields the neutron structure factor for each of these glasses.

To decode the linkages between ring size distribution and FSDP, we then use the measured neutron structure factors to uncover the atomic structure of these glasses by adopting the force-enhanced atomic refinement (FEAR) method [10]. The FEAR modeling approach relies on an iterative combination of RMC refinement and energy minimization cycles. As such, by

43

leveraging all the available information (i.e., both the interatomic forcefield and experimental data), the FEAR approach yields glass structures that simultaneously exhibit excellent match with experimental signatures and high thermodynamic stability [8]. Importantly, FEAR has been shown to offer glass structures that correspond to slowly quenched glasses and yield an improved description of glasses' medium-range order as compared to conventional MD melt-quench simulations [8].

Here, we implement the FEAR approach following Ref. [8] to reveal the atomic structure of glassy silica and Jade(R)—wherein the RMC cycles are conducted by using as constraint the neutron pair distribution functions measured herein (see Methods section). For comparison, these two glasses are also simulated by conventional melt-quench MD simulations (see Methods section). Figure 1 shows the experimental and computed reduced structure factor $F(Q)$ (where $F(Q) = Q \cdot [S(Q) - 1]$, $S(Q)$ being the structure factor) for the silica and Jade glasses. We observe that the FEAR-derived structure factors exhibit an excellent agreement with experimental data over the entire Q range—which is not surprising since the neutron pair distribution functions are used as input for the FEAR simulations. In contrast, the MD-derived structure factors present some notable discrepancies with experimental data. In detail, the level of agreement between MD and experimental data is satisfactory in the high-Q region ($Q \geq 4$Å) (see Figure 1 (a-I) & (b-I)), which suggests that MD offers a decent prediction of the short-range order structure. However, the low-Q peaks are not well reproduced by MD (see Figure 1 (a-II) and (b-II)), which indicates that MD fails at predicting a realistic medium-range order structure (especially for glassy silica). The realistic nature of the glassy structures generated by FEAR is further confirmed by their low energy (as compared to the structures obtained by MD), which denotes their thermodynamic stability (see Methods). The fact that FEAR offers an excellent description of the FSDP of the structure factor of both glasses (significantly improved as compared to MD) offers confidence in the ability of this simulation approach to yield a realistic description of the glasses' medium-range order and, especially, of their ring size distribution.

44
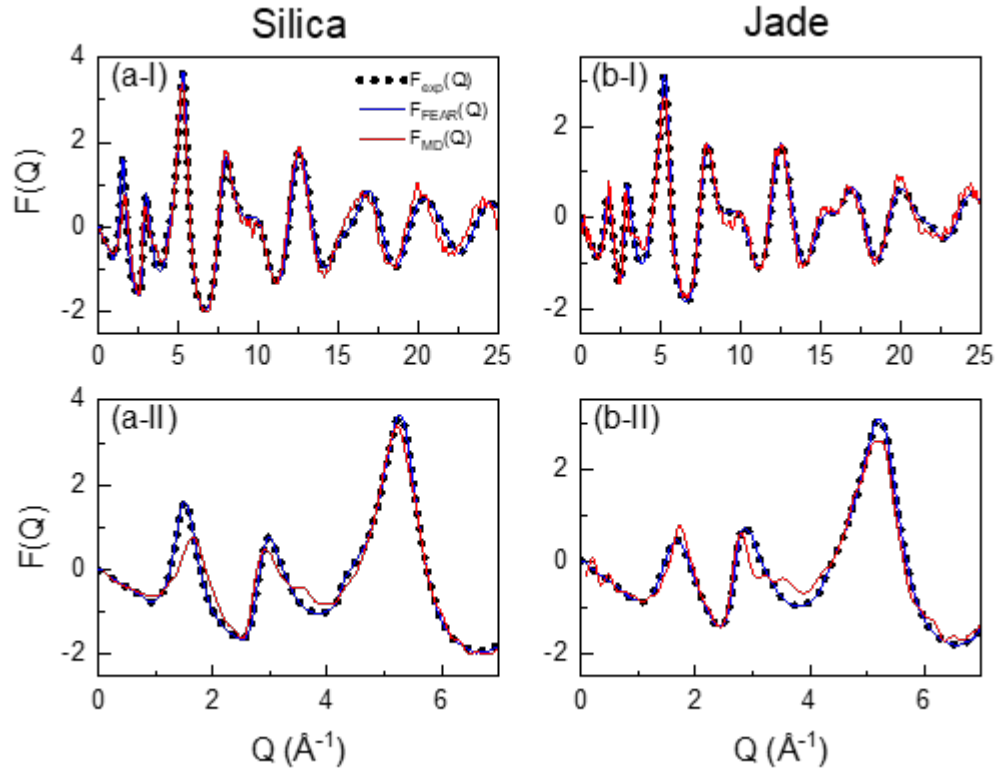
Figure 4.1: Measured and simulated total reduced structure factors (F(Q)) of (a) silica and (b) Jade® glasses. The neutron experimental data are compared with simulation data obtained by FEAR and MD. In both cases, F(Q) derived by FEAR simulation (blue solid curve) matches well with neutron F(Q) (black dot curve), while significant discrepancy is observed for those of MD simulation (red solid curve), especially in low-Q region ($Q \leq 4\text{Å}^{-1}$) as shown in panels (a-II) and (b-II).

Contribution of individual ring sizes to the FSDP

Having established the realistic nature of the glassy structures generated by FEAR, we now use these model structures to decipher how each type of ring contributes to the FSDP. As a prerequisite to this analysis, we discuss the role played by the various definitions that have been proposed for "rings." The very first ring definition—from King—was published in 1967 and defined a ring as the shortest path between two of the nearest neighbors of a given node—for silica, this refers to two oxygen atoms that are connected to a central silicon atom [13]. The King's definition was mostly used in the early studies revolving around ring size analysis [4] [14]. In 1990, Guttman proposed a different way of ring definition for silica materials by using the same shortest path concept. He first simplified the rings as being formed by Si atoms only. He then defined a ring as the shortest path that comes back to a given node (Si atom) starting from one of its nearest-neighbor Si atoms [15]. Since Guttman's criterion uses only one silicon nearest-neighbor as the reference to search the shortest path ring, only the small-size rings (nmax 7 for silica glasses, wherein the ring size n is defined as the numbers of Si atoms in a ring) fulfill Guttman's definition. The large rings (n ¿ 8) that are identified by King's method, are not counted as Guttman rings, as illustrated in Ref. [16]. In that regard, Guttman's rings can be considered as a subset of King's rings, wherein both types of ring originated from the same "shortest path" definition. The third ring definition—primitive—was first introduced by Goetzke and Klein [17] in 1991 and then further developed by Yuan and Cormack [18] in 2002. Primitive rings adopt a different definition as rings that cannot be decomposed into two smaller rings. Another definition—strong ring—was extended from the primitive ring definition, wherein strong rings are not the sum of smaller rings. Therefore, strong rings are a subset of primitive rings, wherein both types of rings originated from the same "indecomposable ring" definition.

In the context of ring size analysis, the RINGS code published in 2010 by Le Roux [16] has been widely used. To describe the connectivity of topological networks, RINGS provides five ways for ring counting, named: (i) all-rings (no rules), (ii) Guttman's, (iii) King's,

(iv) primitive, and (v) strong. Two definitions—all-rings and strong—are not adapted to enumerate rings in glassy structures. Indeed, the all-rings definition enumerates all the rings without adopting any rules, which, in turn, results in an over-counting of the large-size rings [13]. The strong-rings is a technically valid definition, but, in practice, does not apply to large disordered networks. Since strong rings are a subset of primitive rings, searching for strong rings can be performed by finding the strong rings among the primitive rings. However, such strategy only applies to simple crystal structure, whereas, in turn, the ring search tends to diverge for complex disordered structures (see Ref. [16]).

Therefore, only three definitions are eligible for ring size analyses in glass structures. Among RINGS' users, the primitive definition has been almost exclusively adopted [19], [20], [21], at the exception of Ref. [22] wherein the Guttman's definition was used. In most papers focusing on rings, no reasons are provided as to why a specific definition is adopted. Here, in order to uncover which one of these three definitions is relevant to describe the ring size distribution derived from the FSDP of scattering patterns, we compute the King's, Guttman's, and primitive ring size distributions for each FEAR-generated glass structure (silica and Jade). Results are plotted in Figure 2. We find that the three definitions yield the same numbers of small size rings ($n \leq 5$), while we note the existence of differences starting from 6-membered rings. Overall, the Guttman's criterion yields the lowest total number of rings and the identified rings feature a maximum ring size of 7. In contrast, the King's criterion offers the largest total number of rings, including a large portion of large rings (up to $n = 10$). The total number of rings that are computed based on the primitive definition lies in between those yielded by the Guttman's and King's criteria. These differences illustrate the critical role played by the definition that is used when computing rings.

Note that these three definitions yield the same number of small size rings ($n\ leq 5$), while some divergences are observed starting from 6-membered rings. The Guttman's criterion (black) yields the lowest total number of rings and a maximum ring size of 7. The King's criterion (red) yields the highest total number of rings. The total number of primitive rings
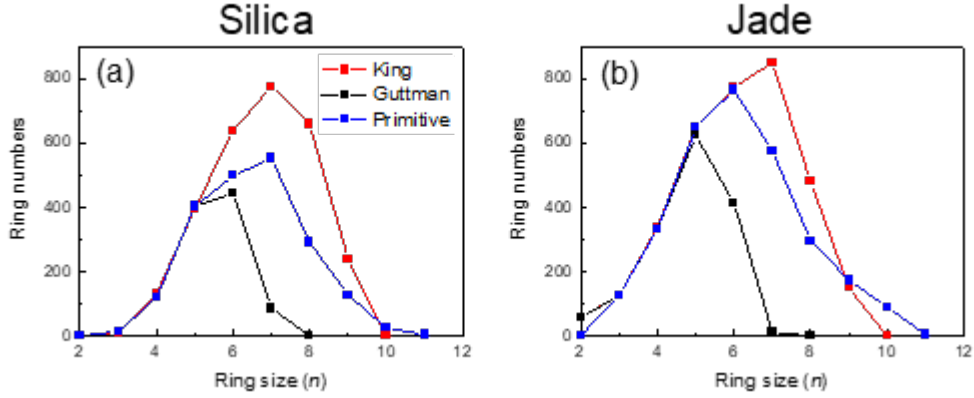
Figure 4.2: King's, Guttman's, and primitive ring size distributions in (a) silica and (b) Jade® glasses.

(blue) lies in between the number of rings identified by the Guttman's and King's definitions.

In the following, we argue that the Guttman's ring definition is the most relevant to describe the ring distribution derived from the FSDP of scattering patterns in terms of the probed length scale. The FSDP originates from medium-range order patterns within the glass structure that are associated with real-space typical repetition distances ranging from 3 to 4.5 Å. This range of distances matches with the typical diameter of the small-size rings ($n \leq 7$) that are identified by Guttman's criterion, whereas, in contrast, the large rings (n geq 8) that are identified by the King's and primitive definitions are associated with larger diameters and, hence, would be only very weakly captured by the FSDP. In addition, as another important point, the Guttman definition yields a realistic total number of rings per network-forming atom, namely, 5.8 and 6.5 for the silica and Jade glasses, respectively. These numbers match with the value of 6 that is expected for fully-polymerized glasses [13]. In contrast, the King's and primitive definitions yield two-to-three times more rings, which suggests that some of these rings are redundant. The method that is used herein to calculate the total number of rings per network-forming atom is described in the Appendix B of Ref. [9]. Based on these reasons, in the following, we systematically adopt the Guttman's definition for this study—since it matches with the typical length scale that is probed by the FSDP and properly reflects the polymerization nature of the networks considered herein.

However, note that this definition may not be appropriate for other types of structural characterization, for instance, to track the large-size primitive rings (n > 10) forming in the alkali-rich silicate glasses [18].

Based on the ring size distributions as shown in Figure 3 (a-I) and (b-I), we investigate the contribution of each type of ring to the structure factor. This is achieved by isolating the selected family of ring, removing the other types of ring (as well as network modifiers) from the simulated structures, and finally calculating the associated partial pair distributions. Using this approach, we compute the individual pair distribution functions associated with fixed ring sizes n (with n = 3-to-7) and grouped pair distribution functions associated with groups of rings (i.e., $\leq$ 4, 5 and $\geq$ 6-membered rings, which follows the group definitions used in the RingFSDP method [9]). The computed reduced pair distribution functions $G_n(r)$ associated with individual and grouped rings are shown in Figure 3 (a-II and b-II, a-III and b-III), respectively.

We then compute the associated reduced structure factors $F_n(Q)$ by Fourier transformation of the individual and grouped pair distribution function $G_n(r)$. Note that 3- (for glassy silica) and 7-membered rings (for Jade) are excluded from this analysis as the low number of such rings (< 20) does not allow for a statistically meaningful analysis. Figure 4 shows the computed individual reduced structure factors $F_n(Q)$ associated with each ring size, along with the neutron diffraction data. Note that, at this point, we solely focus on the positions of the peaks, since the decomposition of the structure factor into contributions from different ring sizes renders the peaks' intensity meaningless. We first note that, in the high-Q range (Q > 4 Å^{-1}), the computed structure factors of both glasses present peaks that are all located at the same positions. This indicates that the different types of rings exhibit fairly similar short-range orders (namely, the structure of the SiO4 and AlO4 polytopes does not depend on the ring size)—which echoes the fact that the peak positions in the low-r region (r < 3 Å) of the pair distribution functions are unaffected by the ring size (see Figure 3 (a-II and b-II)). However, interestingly, we observe that the computed structure factors exhibit some
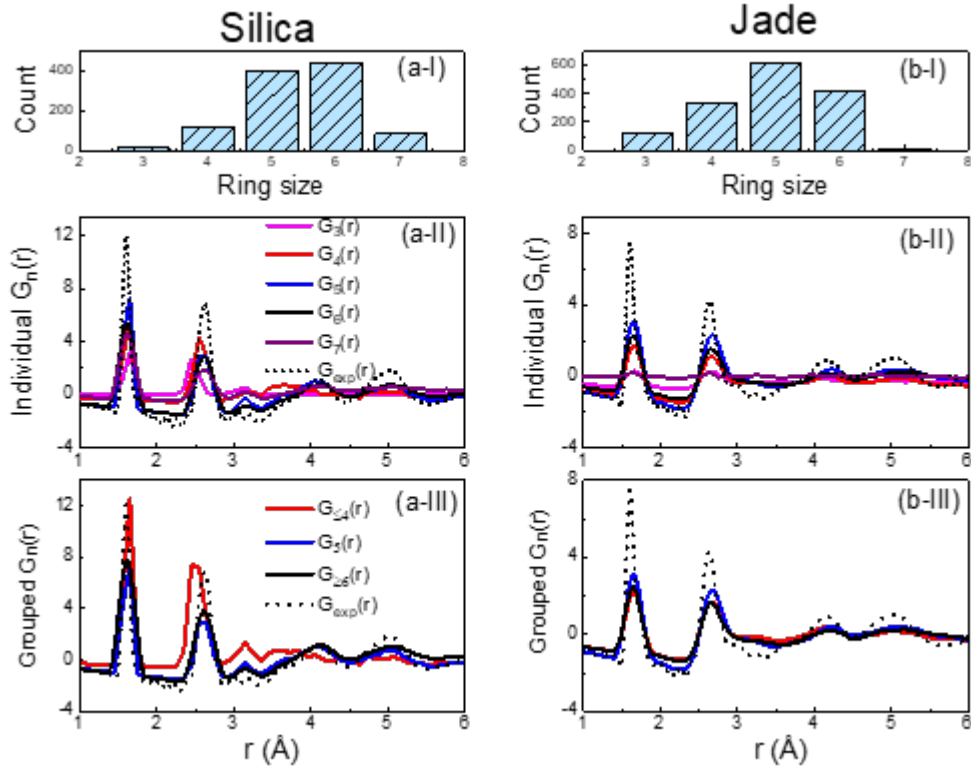
Figure 4.3: Guttman's ring size distribution (I), reduced pair distribution function Gn(r) of individual (II) and grouped (III) rings computed from the FEAR simulations. Note the individual pair distribution functions are associated with fixed ring sizes n (with n = 3-to-7), while grouped pair distribution functions are associated with groups of rings (i.e., $\leq$ 4-, 5 and $\geq$ 6-membered rings, as defined in the RingFSDP method). They are compared to the experimental neutron data (black dot curve).

notable differences in the low-Q region, at the vicinity of the FSDP (see Figure 4 (a-II and b-II)). In both glasses, we find that the position of the FSDP in the individual structure factors systematically shifts toward higher-Q values upon decreasing ring size. This echoes the fact that smaller rings present lower diameter and, hence, are associated with lower typical repetition distances. These simulation results demonstrate that the ring size distribution is encoded in the position and shape of the FSDP—so that, in turn, the deconvolution of the FSDP indeed offers a robust mean to uncover the ring size distribution of glasses based on their diffraction pattern (which is the basis of the RingFSDP method).

Contribution of ring size groups to the FSDP

When deconvoluting experimentally measured FSDPs, simultaneously considering all the ring sizes presented in Figure 4 (i.e., 3-to-7) would require a large number of fitting parameters, which would render the deconvolution impossible. The RingFSDP method was empirically developed from the analysis of 81 aluminosilicate glasses [9]. Each FSDP was fitted in its real-space representation, by two-, three-, and four-Gaussian distributions with all parameters being refined (including peak position, width, and intensity). Two-Gaussian distributions only offer reasonable fittings for glasses containing low silica contents (which exhibit small sized-rings), but not for silica-rich glasses (especially glassy silica) which tend to contain larger populations of large sized-rings. Then, it is determined that three-Gaussian distributions, corresponding to three groups of rings, is the minimum number to fit all the 81 glasses with satisfactory agreement with neutron measured FSDP. It is also found that the positions of three-Gaussian distributions always converge to constant values, i.e., 3.15 ± 0.01, 3.70 ± 0.03, and 4.30 ± 0.04 Å, respectively, where the mean and standard deviation values are calculated from 81 glass fittings. Four-Gaussian distributions definitely improves the fitting quality for silica-rich glasses. For example, the low-Q side of FSDP from glassy silica (Figure 5 (a-II)) can be fitted much better by adding a forth Gaussian peak. However, the increased number of fitting parameters also leads to unrobust and unreliable fitting.

Therefore, the RingFSDP method is based on the core concept that the contributions
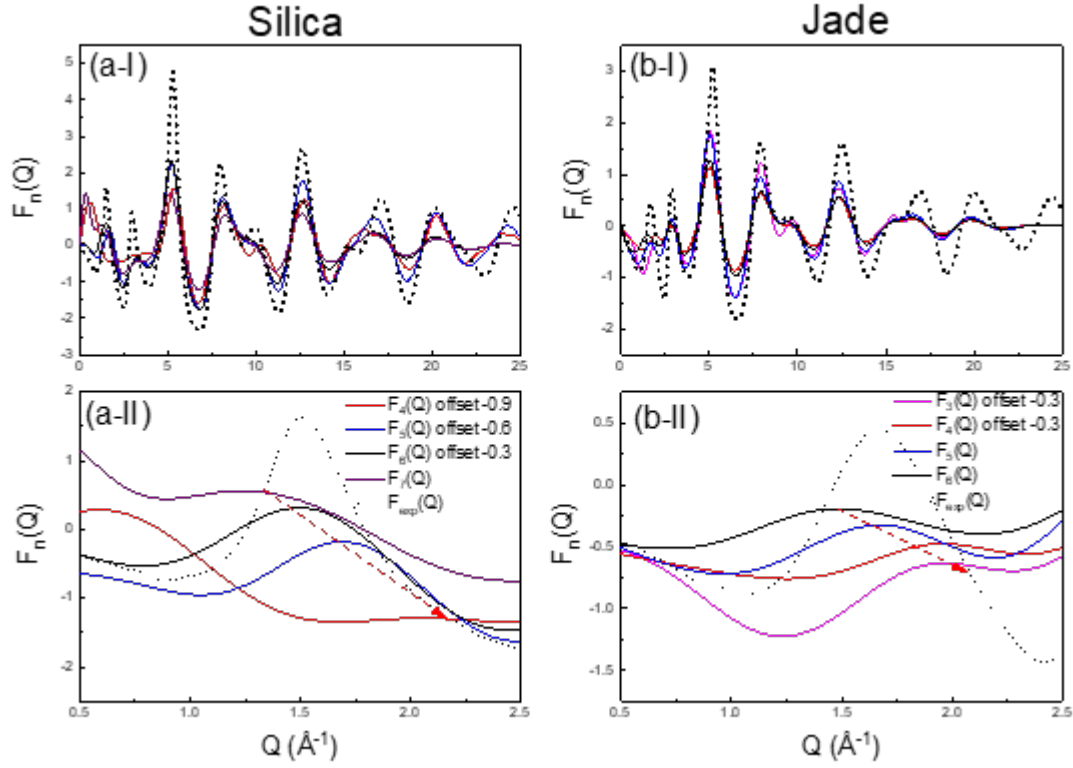
Figure 4.4: Individual reduced structure factor Fn(Q) associated with individual ring size for (a) silica and (b) Jade glasses computed from the FEAR-based glass structures. All four panels adopt the same color scheme for different n-membered rings with the legend shown in panels (a-II) and (b-II). In the whole range panels of FS (a-I) and Jade (b-I), resemblances are shown for the same high-Q peaks $(Q > 4 \text{ Å}^{-1})$ from different sized rings, with their positions in the vicinity range of the corresponding neutron F(Q) peaks (black dot curve). Panels (a-II) and (b-II) show a zoom on the low-Q domain, in which the structure factors are vertically shifted with respect to each other to improve readability and the red arrows aim to guide the eye so as to visualize the shift in the position of the FSDP.

52

to the FSDP of these three groups of rings are located at different fixed-Q positions—so that the deconvolution of the FSDP enables the quantification of the fraction of these three families of rings [9]. As such, in the following, we solely focus on the enumeration of grouped families of rings (i.e., *leq* 4-, 5- and *geq* 6-membered rings, in line with the original RingFSDP method). To support this approach, we compute each structure factor of these three groups of rings from the FEAR model. Figure 5 shows the FSDP in the computed three grouped structure factors, wherein, for clarity, a linear background is subtracted from the computed structure factors to better isolate the FSDP peak. Once again, we find that the FSDPs in these three grouped structure factors are located at notably distinct positions—wherein the FSDP associated with small ($\leq$ 4) and large ring groups ($\geq$ 6) are systematically located at larger and lower Q positions than for the intermediate (5-membered) rings, respectively. Importantly, the positions of the FSDPs of the three grouped structure factors calculated from FEAR-based structures (Figure 5 (a-I) and (b-I)) exhibit a very good agreement with the three fixed-Q values (Figure 5 (a-II) and (b-II)) that were empirically derived from the FSDP deconvolution of 81 silicate glasses [9]. These three Q values correspond to the real-space typical repetition distances 3.15 ± 0.01, 3.70 ± 0.03, and 4.30 ± 0.04 Å, which correspond to the typical effective diameter of small, intermediate, and large rings, respectively [9]. This verifies our first assumption and strongly supports the core concept behind the RingFSDP method.

Based on the grouped structure factor computed from the FEAR-based glass structures, we find that the FSDPs associated with the three groups of rings exhibit a fairly similar peak location in the silica and Jade glasses (see Figure 6). Intuitively, this seems surprising since the rings found in glassy silica solely comprise Si–O bonds (1.62 Å), whereas, in contrast, Jade glasses also present slightly longer Al–O bonds (1.74 Å). Nevertheless, the analysis of the simulated structures reveals that the larger Al–O bonds are compensated by smaller Al–O–Si or Al–O–Al angles [5] so that, overall, the A–A distance (wherein A = Si or Al) remains fairly constant (around 3.1 Å). The value of this A–A distance appears to be a
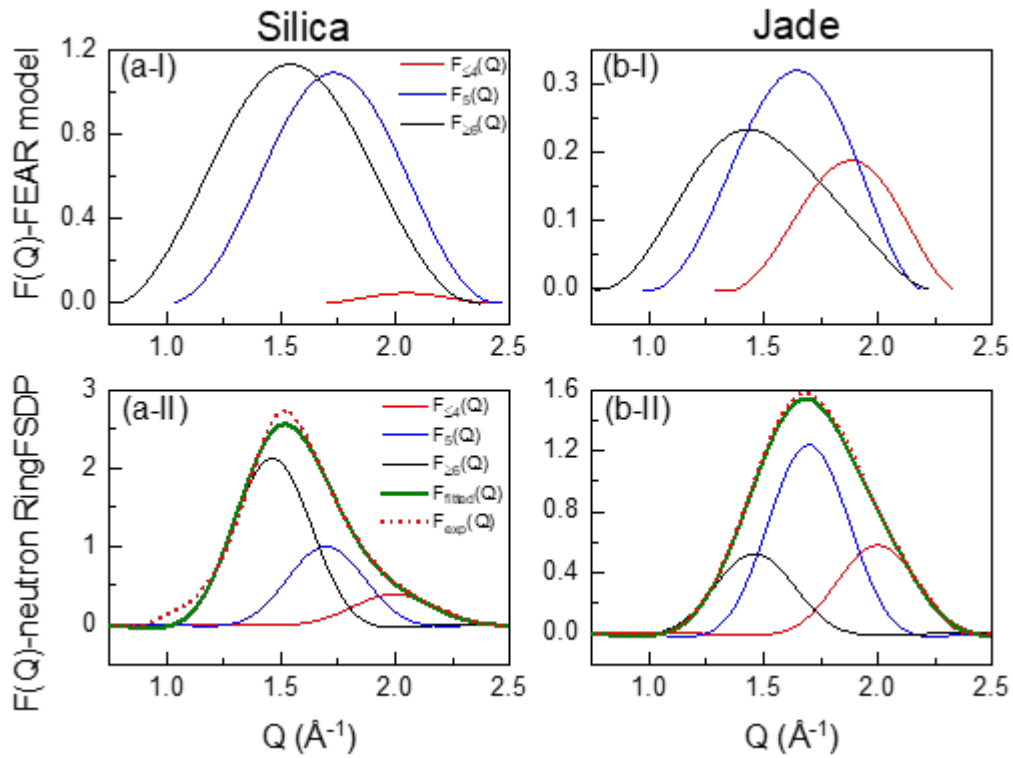
Figure 4.5: Deconvolution of the FSDP into contributions from different ring size groups. The grouped Fn(Q)-FSDP contributions computed from FEAR-based glass structure match with Fn(Q) deconvoluted by RingFSDP method for (a) silica and (b) Jade glasses. For clarity, in panels (a-I) and (b-I) a linear background is subtracted from the computed structure factors to better isolate the FSDP peak. Panels (a-II) and (b-II) show the decomposition of the experimental FSDP following the RingFSDP approach.
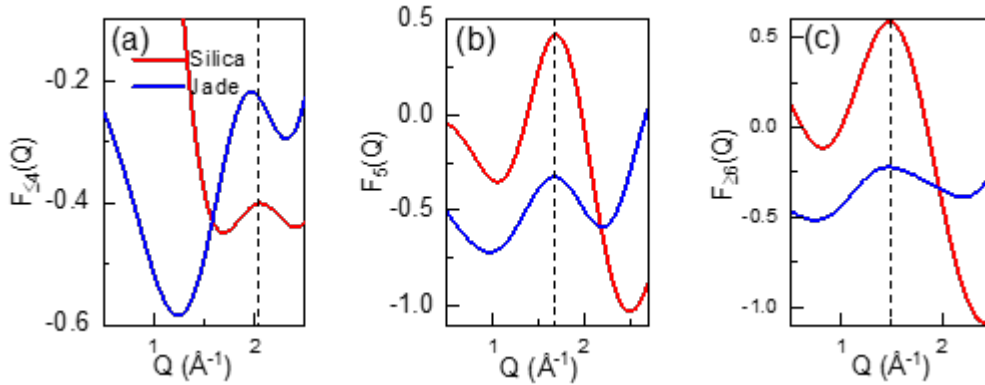
Figure 4.6: Same FSDP positions from same ring size groups regardless of former identities. The Fn(Q) -FSDP derived by FEAR simulation for silica (red) and Jade® (blue) glasses from the same ring size group are shown in (a) ≤4-membred, (b) 5-membred and (c) ≥6-membred. The similar peak positions are observed in all three panels as guided by straight black dot line except a little difference for ≤4-membred ring groups, indicating the ring size is independent of the former identities which comprised the ring.

generic feature of oxide phases based on tetrahedral polytopes, including both crystalline and amorphous SiO_2 and GeO_2 [23], alkaline-earth aluminosilicate glasses [5] [24], as well as 39 tectosilicate crystalline materials with a wide range of Si/Al ratios and very different framework structures ranging from open-structured zeolites to densely-packed coesite SiO_2 [25]. The generality of the A–A distance suggests that, in oxide glasses, the A–O–A angle tends to adapt its average value to achieve a constant A–A distance (rather than the A–A distance being determined by the A–O–A angle). This observation is important since it suggests that the perimeter (and effective diameter) of the rings is not notably affected by the type of network former they are made of. As such, this supports the fact that the positions of the three Gaussian distributions used to deconvolute the FSDP are constant and do not significantly depend on the glass composition—which, in practice, is an important prerequisite to applying the RingFSDP method [9]. Indeed, this implies that the reliable deconvolution of the FSDP only involves six fitting parameters (i.e., the intensity and widths of the three Gaussian distributions) rather than nine (i.e., if 3 additional fitting parameters were to be needed for the positions).

Revealing the ring size distribution in silicate glasses. Finally, having established a robust foundation behind the RingFSDP method, we now apply this approach to deconvolute the FSDP in the experimental neutron structure factor to uncover the fractions of the three groups of rings in the silica and Jade glasses. The decomposition of the FSDP is illustrated in Figure 5 (a-II) and (b-II). In the case of the Jade glass, we find that the combination of the three Gaussian distributions offers an excellent fit of the FSDP. Although a satisfactory fit is also obtained in the case of glassy silica, we nevertheless observe some fitting discrepancy in the low-Q range (around 1 Å-1) of the FSDP. The fitting could be improved by considering an additional group of very large rings ($\geq$ 7-membered rings). However, adding a fourth Gaussian distribution would increase the number of fitting parameters and, hence, negatively affect the reliability of the deconvolution of the FSDP—so that we stick to the above mentioned three groups of rings. The fractions of each group of rings are then determined based on the areas under these three fitted distributions (see Figure 7). Overall, we find that glassy silica exhibits most large rings ($\geq$ 6-membered), while, in contrast, Jade exhibits an excess of 5-membered rings. The results obtained for Jade echo the ring size distribution that was reported for another fully compensated aluminosilicate glass $(CaO)13.5(Al2O3)13.5(SiO2)73$ [9]. Importantly, these observations match with the outcomes of the direct enumeration of the rings based on the analysis of the glass structures simulated by FEAR (see Figure 7). We also note that, in the case of glassy silica, the ring size distribution obtained herein matches with previous MD simulation results from Vashishta et al. [4] (see Figure 7). We compare our results with Vashishta's because the S(Q) calculated from their MD simulation matches well with the measured pattern obtained by neutron diffraction, especially in the FSDP region (as shown in Figure 1 of Ref. [4]). This indicates that their MD simulation yields a more realistic medium-range order structure than that predicted by the BKS forcefield used herein (see Figure 1 (a-II)). This improved level of agreement is likely on account of the fact that, unlike the present BKS forcefield, the Vashista forcefield is a complex potential that features 3-body energy terms.
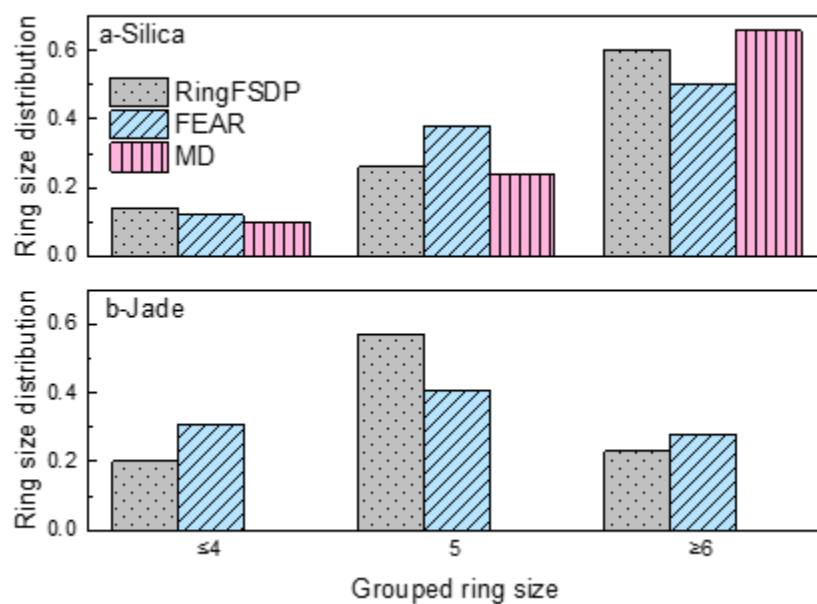
Figure 4.7: Ring size distribution comparison between the experimental RingFSDP and FEAR/MD simulation analysis. The good match between experiment and modeling validates the RingFSDP method.

Conclusion Although the RingFSDP method is necessarily incomplete since it is limited to small ring sizes (n $\leq$ 7), many studies (detailed in the following) have highlighted the unique and critical role played by small size rings in glasses. As such, quantifying the number of small rings is key to decipher the nature of composition-structure-properties correlation in glasses and accelerate the development of new glass compositions with tailored functionalities. Specifically, our previous in situ neutron scattering study on fused silica (FS) revealed that the intensity of the FSDP associated with small size rings (n $\leq$ 4) decreases more than those associated with large-sized rings upon increasing temperature [26]. This denotes that small rings are fairly unstable, which echoes several recent observations: (i) small-size rings (n = 3 and 4) are energetically unfavorable since they present much higher relative energies as compared to that of 6-membered rings in FS [4], (ii) small size rings (n < 6) in sodium silicate glass (0.3Na2O·0.7SiO2) exhibit some significant internal stress on account of their over constrained topological nature, whereas large-sized rings (n $\geq$ 6) do not [27], (iii) MD simulations echo our experimental in situ observations, namely, when alkaline or alkaline-earth silicate glasses are heated above their respective glass transition temperature, small-sized rings (n $\leq$ 4) show more dramatic change as compared to their larger counterparts (n $\geq$ 5) [21].

Altogether, the overall harmony between the experimental (i.e., obtained from the deconvolution of the FSDP) and simulated results (i.e., obtained from a direct enumeration of the rings) that are reported herein strongly supports the soundness of the RingFSDP approach. This is significant as, to the best of our knowledge, this approach is the only method enabling a direct estimation of the ring size distribution in silicate glasses, while solely relying on experimental diffraction data.

CHAPTER 5

Summary

Despite the extraordinary importance of amorphous materials in our daily lives and the many chances of exploring new materials to address many of the essential challenges for the future development, current research on glassy materials remains weak. Much of the research being conducted–such as molecular dynamics simulation of the transition for the glass in purely model systems without evolving any real chemistry–is insufficient to solve practical problems in real world materials14.

For previous research, we have introduced a new and practical method that enables the combination of experimental information and the total-energy calculation. FEAR approach provides us new tool to solve the old problem of structural inversion of diffraction data. The whole ideal for the method is simple and robust. The convergence of Wright's cost function and total energy between two distinct systems. The method is unbiased since that it starts with a completely random configuration and with a total-energy functional aided by additional experimental information to reach a stable state. On the other hand, concrete nanoengineering becomes important and may lead to the future development in cement and concrete technology. Although nowadays, the technology remains poorly defined, with the combination of experimental, numerical, and theoretical approaches, we can explore new method to characterize how the nanoscale structure of concrete can be tuned to design concretes with wanted macroscopic properties, or even reduce the carbon emission98.

REFERENCE

1. Mauro, J. C. & Zanotto, E. D. Two Centuries of Glass Research: Historical Trends, Current Status, and Grand Challenges for the Future. Int J Appl Glass Sci 5, 313–327 (2014).

2. Tribello, G. A., Bruneval, F., Liew, C. & Parrinello, M. A Molecular Dynamics Study of the Early Stages of Calcium Carbonate Growth. The Journal of Physical Chemistry B 113, 11680–11687 (2009).

3. Du, T., Li, H., Sant, G. & Bauchy, M. New insights into the sol–gel condensation of silica by reactive molecular dynamics simulations. The Journal of Chemical Physics 148, 234504 (2018).

4. Li, X., Song, W., Smedskjaer, M. M., Mauro, J. C. & Bauchy, M. Quantifying the internal stress in over-constrained glasses by molecular dynamics simulations. Journal of Non-Crystalline Solids: X 1, 100013 (2019).

5. Bauchy, M. Structural, vibrational, and elastic properties of a calcium aluminosilicate glass from molecular dynamics simulations: The role of the potential. The Journal of Chemical Physics 141, 024507 (2014).

6. Proffen, Th., Billinge, S. J. L., Egami, T. & Louca, D. Structural analysis of complex materials using the atomic pair distribution function — a practical guide. Zeitschrift für Kristallographie - Crystalline Materials 218, (2003).

7. Yu, Y., Mauro, J. C. & Bauchy, M. Stretched exponential relaxation of glasses: Origin of the mixed-alkali effect. American Ceramic Society Bulletin 96, 34–36 (2017). 8. Ferlat, G., Soetens, J.-C., Miguel, A. S. & Bopp, P. A. Combining extended x-ray absorption fine structure with numerical simulations for disordered systems. Journal of Physics: Condensed Matter 17, S145–S157 (2005).

9. Liu, Z. et al. Glass relaxation and hysteresis of the glass transition by molecular dynamics simulations. Phys. Rev. B 98, 104205 (2018).

10. Du, J. & Cormack, A. N. The medium range structure of sodium silicate glasses: a

molecular dynamics simulation. Journal of Non-Crystalline Solids 349, 66–79 (2004).

11. Yu, Y. et al. Hardness of silicate glasses: Atomic-scale origin of the mixed modifier effect. Journal of Non-Crystalline Solids 489, 16–21 (2018).

12. Du, T. et al. Atomistic origin of the passivation effect in hydrated silicate glasses. npj Materials Degradation 3, (2019).

13. Li, X. et al. Cooling rate effects in sodium silicate glasses: Bridging the gap between molecular dynamics simulations and experiments. The Journal of Chemical Physics 147, 074501 (2017).

14. Bauchy, M. Structural, vibrational, and thermal properties of densified silicates: Insights from molecular dynamics. The Journal of Chemical Physics 137, 044510 (2012).

15. Song, W. et al. Atomic picture of structural relaxation in silicate glasses. Appl. Phys. Lett. 114, 233703 (2019).

16. Committee on Developing a Research Agenda for Utilization of Gaseous Carbon Waste Streams, Board on Chemical Sciences and Technology, Division on Earth and Life Studies, & National Academies of Sciences, Engineering, and Medicine. Gaseous Carbon Waste Streams Utilization: Status and Research Needs. (National Academies Press, 2019). doi:10.17226/25232.

17. Wei, Z. et al. Clinkering-free cementation by fly ash carbonation. Journal of CO2 Utilization 23, 117–127 (2018).

18. Ogino, T., Suzuki, T. & Sawada, K. The formation and transformation mechanism of calcium carbonate in water. Geochimica et Cosmochimica Acta 51, 2757–2767 (1987).

19. Jaschik, J., Jaschik, M. & Warmuziński, K. The utilisation of fly ash in CO2 mineral carbonation. Chemical and Process Engineering 37, (2016).

20. Bauchy, M., Qomi, M. J. A., Ulm, F.-J. & Pellenq, R. J.-M. Order and disorder in calcium–silicate–hydrate. The Journal of Chemical Physics 140, 214503 (2014).

21. Abdolhosseini Qomi, M. J. et al. Combinatorial molecular optimization of cement hydrates. Nature Communications 5, (2014).

22. Bauchy, M., Qomi, M. J. A., Ulm, F.-J. & Pellenq, R. Is Cement a Glassy Material?

arXiv:1506.06445 [cond-mat] (2015).

23. McGreevy, R. L. & Pusztai, L. Reverse Monte Carlo Simulation: A New Technique for the Determination of Disordered Structures. Molecular Simulation 1, 359–367 (1988).

24. Biswas, P., Atta-Fynn, R. & Drabold, D. A. Reverse Monte Carlo modeling of amorphous silicon. Physical Review B 69, (2004).

25. Pandey, A., Biswas, P. & Drabold, D. A. Force-enhanced atomic refinement: Structural modeling with interatomic forces in a reverse Monte Carlo approach applied to amorphous Si and SiO 2. Physical Review B 92, (2015).

26. Mauro, J. C. Decoding the glass genome. Current Opinion in Solid State and Materials Science 22, 58–64 (2018).

27. Mauro, J. C., Philip, C. S., Vaughn, D. J. & Pambianchi, M. S. Glass Science in the United States: Current Status and Future Directions. Int J Appl Glass Sci 5, 2–15 (2014).

28. Mauro, J. C. & Zanotto, E. D. Two Centuries of Glass Research: Historical Trends, Current Status, and Grand Challenges for the Future. International Journal of Applied Glass Science 5, 313–327 (2014).

29. Wondraczek, L. et al. Towards Ultrastrong Glasses. Adv. Mater. 23, 4578–4586 (2011).

30. Le Losq, C., Cicconi, M. R., Greaves, G. N. & Neuville, D. R. Silicate Glasses. in Springer Handbook of Glass (eds. Musgraves, J. D., Hu, J. & Calvez, L.) 441–503 (Springer International Publishing, 2019). doi:10.1007/978-3-319-93728-1_13.

31. Yu, Y., Wang, B., Wang, M., Sant, G. & Bauchy, M. Revisiting silica with ReaxFF: Towards improved predictions of glass structure and properties via reactive molecular dynamics. Journal of Non-Crystalline Solids 443, 148–154 (2016).

32. Biswas, R. K. et al. Study of short range structure of amorphous Silica from PDF using Ag radiation in laboratory XRD system, RAMAN and NEXAFS. Journal of Non-Crystalline Solids 488, 1–9 (2018).

33. Sørensen, S. S., Biscio, C. A. N., Bauchy, M., Fajstrup, L. & Smedskjaer, M. M. Revealing hidden medium-range order in amorphous materials using topological data analysis.

Sci. Adv. 6, eabc2320 (2020). 34. Elliott, S. R. Medium-range structural order in covalent amorphous solids. Nature 354, 445–452 (1991). 35. Shi, R. & Tanaka, H. Distinct signature of local tetrahedral ordering in the scattering function of covalent liquids and glasses. Sci. Adv. 5, eaav3194 (2019).

36. Huang, P. Y. et al. Imaging Atomic Rearrangements in Two-Dimensional Silica Glass: Watching Silica's Dance. Science 342, 224–227 (2013).

37. Yang, Y. et al. Determining the three-dimensional atomic structure of an amorphous solid. Nature 592, 60–64 (2021).

38. Pandey, A., Biswas, P. & Drabold, D. A. Inversion of diffraction data for amorphous materials. Scientific Reports 6, 33731 (2016).

39. Du, J. & Corrales, L. R. First sharp diffraction peak in silicate glasses: Structure and scattering length dependence. Phys. Rev. B 72, 092201 (2005).

40. Du, J. & Corrales, L. R. Compositional dependence of the first sharp diffraction peaks in alkali silicate glasses: A molecular dynamics study. Journal of Non-Crystalline Solids 352, 3255–3269 (2006).

41. Micoulaut, M. & Bauchy, M. Anomalies of the first sharp diffraction peak in network glasses: Evidence for correlations with dynamic and rigidity properties. physica status solidi (b) 250, 976–982 (2018).

42. Shi, Y. et al. Ring size distribution in silicate glasses revealed by neutron scattering first sharp diffraction peak analysis. Journal of Non-Crystalline Solids 516, 71–81 (2019).

43. Molecular Dynamics Simulations of Disordered Materials. vol. 215 (Springer International Publishing, 2015).

44. Lane, J. M. D. Cooling rate and stress relaxation in silica melts and glasses via microsecond molecular dynamics. Phys. Rev. E 92, 012320 (2015).

45. Song, W. et al. Atomic picture of structural relaxation in silicate glasses. Applied Physics Letters 114, 233703 (2019).

46. Du, J. Challenges in Molecular Dynamics Simulations of Multicomponent Oxide Glasses.

in Molecular Dynamics Simulations of Disordered Materials: From Network Glasses to Phase-Change Memory Alloys (eds. Massobrio, C., Du, J., Bernasconi, M. & Salmon, P. S.) 157–180 (Springer International Publishing, 2015). doi:10.1007/978-3-319-15675-0_7.

47. Huang, L. & Kieffer, J. Challenges in Modeling Mixed Ionic-Covalent Glass Formers. in Molecular Dynamics Simulations of Disordered Materials: From Network Glasses to Phase-Change Memory Alloys (eds. Massobrio, C., Du, J., Bernasconi, M. & Salmon, P. S.) 87–112 (Springer International Publishing, 2015). doi:10.1007/978-3-319-15675-0_4.

48. Vollmayr, K., Kob, W. & Binder, K. Cooling-rate effects in amorphous silica: A computer-simulation study. Phys. Rev. B 54, 15808–15827 (1996).

49. Plimpton, S. Computational limits of classical molecular dynamics simulations. Computational Materials Science 4, 361–364 (1995).

50. Bhaskar, P. et al. Cooling rate effects on the structure of 45S5 bioglass: Insights from experiments and simulations. Journal of Non-Crystalline Solids 534, 119952 (2020).

51. Deng, L. & Du, J. Effects of system size and cooling rate on the structure and properties of sodium borosilicate glasses from molecular dynamics simulations. The Journal of Chemical Physics 148, 024504 (2018).

52. Tilocca, A. Cooling rate and size effects on the medium-range structure of multicomponent oxide glasses simulated by molecular dynamics. The Journal of Chemical Physics 139, 114501 (2013).

53. Ito, S. & Taniguchi, T. Effect of cooling rate on structure and mechanical behavior of glass by MD simulation. Journal of Non-Crystalline Solids 349, 173–179 (2004).

54. Tan, J., Zhao, S., Wang, W., Davies, G. & Mo, X. The effect of cooling rate on the structure of sodium silicate glass. Materials Science and Engineering: B 106, 295–299 (2004).

55. McGreevy, R. L. Reverse Monte Carlo modelling. Journal of Physics: Condensed Matter 13, R877–R913 (2001).

56. Bousige, C., Boţan, A., Ulm, F.-J., Pellenq, R. J.-M. & Coasne, B. Optimized molecular reconstruction procedure combining hybrid reverse Monte Carlo and molecular dynamics.

The Journal of Chemical Physics 142, 114112 (2015).

57. Opletal, G. et al. Hybrid approach for generating realistic amorphous carbon structure using metropolis and reverse Monte Carlo. Molecular Simulation 28, 927–938 (2002).

58. Keen, D. A. & McGreevy, R. L. Structural modelling of glasses using reverse Monte Carlo simulation. Nature 344, 423–425 (1990).

59. Müller, C. R., Kathriarachchi, V., Schuch, M., Maass, P. & Petkov, V. G. Reverse Monte Carlo modeling of ion conducting network glasses: An evaluation based on molecular dynamics simulations. Physical Chemistry Chemical Physics 12, 10444 (2010).

60. Drabold, D. A. Topics in the theory of amorphous materials. The European Physical Journal B 68, 1–21 (2009).

61. Zhou, Q., Du, T., Guo, L., Smedskjaer, M. M. & Bauchy, M. New insights into the structure of sodium silicate glasses by force-enhanced atomic refinement. Journal of Non-Crystalline Solids 536, 120006 (2020).

62. Limbu, D. K., Atta-Fynn, R., Drabold, D. A., Elliott, S. R. & Biswas, P. Information-driven inverse approach to disordered solids: Applications to amorphous silicon. Physical Review Materials 2, (2018).

63. Liu, Z. et al. Glass relaxation and hysteresis of the glass transition by molecular dynamics simulations. Phys. Rev. B 98, 104205 (2018).

64. Kramer, G. J., Farragher, N. P., van Beest, B. W. H. & van Santen, R. A. Interatomic force fields for silicas, aluminophosphates, and zeolites: Derivation based on ab initio calculations. Phys. Rev. B 43, 5068–5080 (1991).

65. Yuan, F. & Huang, L. Brittle to Ductile Transition in Densified Silica Glass. Sci Rep 4, 5035 (2015).

66. Hockney, R. W. & Eastwood, J. W. Computer simulation using particles. in (1966).

67. Guillot, B. & Sator, N. A computer simulation study of natural silicate melts. Part I: Low pressure properties. Geochimica et Cosmochimica Acta 71, 1249–1265 (2007).

68. Pedone, A., Malavasi, G., Menziani, M. C., Cormack, A. N. & Segre, U. A New Self-

Consistent Empirical Interatomic Potential Model for Oxides, Silicates, and Silica-Based Glasses. J. Phys. Chem. B 110, 11780–11795 (2006).

69. Plimpton, S. Fast Parallel Algorithms for Short–Range Molecular Dynamics. 42.

70. Hoover, W. G. Canonical dynamics: Equilibrium phase-space distributions. Phys. Rev. A 31, 1695–1697 (1985).

71. Shi, Y. et al. Structural evolution of fused silica below the glass-transition temperature revealed by in-situ neutron total scattering. Journal of Non-Crystalline Solids 119760 (2019) doi:10.1016/j.jnoncrysol.2019.119760.

72. Sears, V. F. Neutron scattering lengths and cross sections. Neutron News 3, 26–37 (1992).

73. Wright, A. C. The comparison of molecular dynamics simulations with diffraction experiments. Journal of Non-Crystalline Solids 159, 264–268 (1993).

74. Le Roux, S. & Jund, P. Ring statistics analysis of topological networks: New approach and application to amorphous GeS2 and SiO2 systems. Computational Materials Science 49, 70–83 (2010).

75. Guttman, L. Ring structure of the crystalline and amorphous forms of silicon dioxide. Journal of Non-Crystalline Solids 116, 145–147 (1990).

76. Debenedetti, P. G. & Stillinger, F. H. Supercooled liquids and the glass transition. Nature 410, 259–267 (2001). 77. Kob, W. & Andersen, H. C. Testing mode-coupling theory for a supercooled binary Lennard-Jones mixture I: The van Hove correlation function. Phys. Rev. E 51, 4626–4641 (1995).

78. Wright, A. C. Neutron scattering from vitreous silica. V. The structure of vitreous silica: What have we learned from 60 years of diffraction studies? Journal of Non-Crystalline Solids 179, 84–115 (1994).

79. Neuefeind, J. & Liss, K.-D. Bond angle distribution in amorphous germania and silica. Berichte der Bunsengesellschaft für physikalische Chemie 100, 1341–1349 (1996).

80. Malfait, W. J., Halter, W. E. & Verel, R. 29Si NMR spectroscopy of silica glass: T1

relaxation and constraints on the Si–O–Si bond angle distribution. Chemical Geology 256, 269–277 (2008).

81. Pettifer, R. F., Dupree, R., Farnan, I. & Sternberg, U. NMR determinations of Si O Si bond angle distributions in silica. Journal of Non-Crystalline Solids 106, 408–412 (1988).

82. Poulsen, H. F., Neuefeind, J., Neumann, H.-B., Schneider, J. R. & Zeidler, M. D. Amorphous silica studied by high energy X-ray diffraction. Journal of Non-Crystalline Solids 188, 63–74 (1995).

83. Gladden, L. F., Carpenter, T. A. & Elliott, S. R. 29 Si MAS NMR studies of the spin-lattice relaxation time and bond-angle distribution in vitreous silica. Philosophical Magazine B 53, L81–L87 (1986).

84. Coombs, P. G. et al. The nature of the Si-O-Si bond angle distribution in vitreous silica. Philosophical Magazine B 51, L39–L42 (1985).

85. Rino, J. P., Ebbsjö, I., Kalia, R. K., Nakano, A. & Vashishta, P. Structure of rings in vitreous SiO 2. Phys. Rev. B 47, 3053–3062 (1993).

86. Huang, P. Y. et al. Direct Imaging of a Two-Dimensional Silica Glass on Graphene. Nano Lett. 12, 1081–1086 (2012). 87. Shi, Y., Zhou, Q., Deng, B. & Bauchy, M. Experimental Method to Quantify the Ring Size Distribution in Silicate Glasses and Simulation Validation Thereof.

88. Varshneya, A. K. Fundamentals of inorganic glasses: Arun K. Varshneya. (Academic Press, 1994).

89. Kamiya, K. & Sakka, S. Thermal expansion of TiO2SiO2 and TiO2GeO2 glasses. Journal of Non-Crystalline Solids 52, 357–363 (1982).

90. Shi, Y. et al. Ring size distribution in silicate glasses revealed by neutron scattering first sharp diffraction peak analysis. Journal of Non-Crystalline Solids 516, 71–81 (2019).

91. Zhou, Q., Shi, Y., Deng, B., Neuefeind, J. & Bauchy, M. Experimental method to quantify the ring size distribution in silicate glasses and simulation validation thereof. Sci. Adv. 7, eabh1761 (2021).

92. Li, X. et al. Cooling rate effects in sodium silicate glasses: Bridging the gap between molecular dynamics simulations and experiments. The Journal of Chemical Physics 147, 074501 (2017).

93. Lane, J. M. D. Cooling rate and stress relaxation in silica melts and glasses via microsecond molecular dynamics. Phys. Rev. E 92, 012320 (2015).

94. Pandey, A., Biswas, P. & Drabold, D. A. Force-enhanced atomic refinement: Structural modeling with interatomic forces in a reverse Monte Carlo approach applied to amorphous Si and SiO_2. Phys. Rev. B 92, 155205 (2015). 95. Zhou, Q. et al. Revealing the medium-range structure of glassy silica using force-enhanced atomic refinement. Journal of Non-Crystalline Solids 573, 121138 (2021).

96. van Beest, B. W. H., Kramer, G. J. & van Santen, R. A. Force fields for silicas and aluminophosphates based on ab initio calculations. Phys. Rev. Lett. 64, 1955–1958 (1990).

97. Bauchy, M. et al. Topological Control on the Structural Relaxation of Atomic Networks under Stress. Physical Review Letters 119, (2017).

98. Ashraf, W. & Olek, J. Carbonation behavior of hydraulic and non-hydraulic calcium silicates: potential of utilizing low-lime calcium silicates in cement-based materials. Journal of Materials Science 51, 6173–6191 (2016).